Deglaciation history and relative sea level changes since the Last Glacial Maximum in the southern Gulf of St. Lawrence, Canada

I. Schulten[1*], V. Maselli[1, 2], E. L. King[3], M. Schmidt[4], C. Hensen[4], T. Müller[4, 5], A. Asioli[6], A. Micallef[7], C. Berndt[4], C. J. Brown[8], F. Córdoba-Ramírez[1], J. Elger[4, 9], S. Hölz[4], A. Kotliarov[10], B. Kurylyk[11], S. Yu[11], M. R. Nedimović[1]

[1] Department of Earth and Environmental Sciences, Dalhousie University, Halifax, Nova Scotia, Canada
[2] Department of Chemical and Geological Sciences, University of Modena and Reggio Emilia, Modena, Italy
[3] Natural Resources Canada (NRCan), Geological Survey of Canada Atlantic, Dartmouth, Nova Scotia, Canada
[4] GEOMAR Helmholtz Centre for Ocean Research Kiel, RD2/Marine Geosystems, RD4/Marine Geodynamic, Kiel, Germany
[5] Department Hydrogeology, Helmholtz Centre for Environmental Research GmbH - UFZ, Leipzig, Germany
[6] Institute of Marine Sciences (CNR-ISMAR), Bologna, Italy
[7] Monterey Bay Aquarium Research Institute (MBARI), Moss Landing, California, USA
[8] Department of Oceanography, Dalhousie University, Halifax, Nova Scotia, Canada
[9] Department of Geoscience, Aarhus University, Aarhus C, Denmark
[10] Fisheries and Marine Institute, Memorial University of Newfoundland, Newfoundland and Labrador, Canada
[11] Department of Civil and Resource Engineering and Centre for Water Resources Studies, Dalhousie University, Halifax, Nova Scotia, Canada

*Corresponding author: irena.schulten@dal.ca

Abstract

During the last glacial period, continents and surrounding shelves in high latitude regions of the Northern Hemisphere were covered by ice sheets. Their retreat during the late Pleistocene and Holocene resulted in isostatic adjustments of the previously glaciated landmass, which influenced post-glacial changes in relative sea level (RSL). Many questions, however, remain about the timing and impact of the ice retreat on the continental shelf environments and RSL after the Last Glacial Maximum, and of short-lived climatic events, such as the Younger Dryas. This study aims to reconstruct the deglaciation history and changes in RSL for the southern Gulf of St. Lawrence off Prince Edward Island on the eastern Canadian continental shelf for the past 14 ka, and to determine the influence of the Younger Dryas on the ice margin. Using information from sub-bottom profiles, sediment cores, and multibeam bathymetry, this study finds that most of the continental shelf was already flooded 13.6 ka ago, as evidenced by the presence of Bølling-Allerød marine sediments at a modern water depth of less than 50 m and ~15 km off the modern coastline. During the Younger Dryas cooling event, sedimentation rates increased from 0.1 to 1 cm a^{-1}, likely as a consequence

of readvancing ice masses. We observe an erosional truncation on top of the Younger Dryas sediment package, which presumably indicates a drop in RSL in the early Holocene. Based on our new data, we propose an updated RSL curve for the region that accounts for the presence of sea ice coverage rather than complete ice coverage as well as a geological model highlighting the sedimentation history over the past 14 ka and role of the Younger Dryas. The new paleo-environmental and RSL reconstructions shed light on the potential impact of short-lived climatic events at the former ice margin during deglaciation and reduce uncertainties for about past sea level changes.

1. Introduction

The Pleistocene glaciations significantly shaped the modern landscape of the Northern Hemisphere. During the last cold period, which culminated in the Last Glacial Maximum (LGM) between 26 and 18 ka BP (Clark et al., 2009), the high latitude regions of North America and their adjacent continental shelves were covered by the Laurentide Ice Sheet (LIS) (e.g., Dyke et al., 2003; Shaw, 2005; Shaw et al., 2006; Stokes, 2017; Dalton et al., 2020). The glaciations left behind specific depositional and erosional features, both onshore and offshore, which provide essential information about the ice dynamics (Shaw et al., 2006; 2009; Winsborrow et al., 2010; Evans & Evans, 2022). Over the past few decades, several studies aimed to quantify how the LIS advanced and retreated, especially following the LGM (e.g., Fairbanks, 1989; Dyke et al., 2003; Stea, 2011; Stokes, 2017; Dalton et al., 2024). The impact of short-lived climatic oscillations on the ice sheet dynamics, such as the Younger Dryas cooling event (12.9-11.6 ka BP), are, however, still debated (e.g., Loring & Nota, 1973; Fairbanks, 1989; Stea & Mott, 1989; 1998; Dyke et al., 2003; Stokes, 2017; Dalton et al., 2024). Ice retreat at the end of the last glaciation caused isostatic adjustments in many high latitude regions. Over time, a collapse of the forebulge margin and hydro-isostatic loading along coastlines instigated subsidence of the former glaciated margins such as observed in parts of eastern Canada (Forbes et al., 2014), and many regions still experience a rise in relative sea level to this day (RSL; IPCC, 2023). A precise quantification of the extent and retreat history of the former ice sheets, particularly along their margins (i.e., the modern continental shelves) is therefore key to improving our current understanding about ice sheet dynamics and associated RSL changes.

In our study area, the southern Gulf of St. Lawrence offshore Prince Edward Island (PEI) in Eastern Canada (Fig. 1a), a retreat of the LIS following the LGM is presumed to have resulted in an early RSL drop due to isostatic uplift (Shaw, 2005; Forbes et al., 2004; 2014; Shaw et al., 2006; 2009; Vacchi et al., 2018). Ice sheet retreat was likely interrupted during the Younger Dryas, when a short-lived ice re-advance or ice buildup may have occurred (Shaw, 2005; Shaw et al., 2006; 2009; Vacchi et al., 2018). Its exact extent and influence on sedimentation and RSL for this region is, however, highly debated (e.g., Loring & Nota, 1973; Stea & Mott, 1989; 1998). Following the Younger Dryas, the margin likely experienced a rise in RSL starting at ~9 ka BP in response to isostatic subsidence related to movement of the forebulge margin (Forbes et al., 2004; 2014). This subsidence and RSL rise persists until today at a rate of 3.2 mm a^{-1}, which is much faster than the global average (Carr, 1969; Forbes et al., 2004; Barlow & Reichard, 2010). The high rate of RSL rise causes significant problems to coastal communities situated in the region as it increases their vulnerability to coastal flooding, erosion, and saltwater intrusion (SWI) into onshore aquifers (Forbes et al., 2014; Stanic et al., 2024).

Open questions remain regarding the sedimentation history in the southern Gulf of St. Lawrence since the LGM, the influence and extent of the Younger Dryas, and how it influenced changes in RSL especially between the LGM and the onset of the Holocene. This information is important to improve current models for RSL reconstructions and predictions for Atlantic Canada. In this study, we therefore aim to reconstruct the deglaciation history and associated changes in RSL in the southern Gulf of St. Lawrence following the LGM by identifying changes in sedimentation patterns and paleo-environments using newly acquired multibeam bathymetry, sub-bottom seismic profiles and sediment cores (Figs. 1b & c, S1, S2). The new findings will improve environmental reconstructions for the region and provide key information about paleo-ice limits and buried drainage systems. The information can be useful also to understand the connection between onshore and offshore aquifers (cf. Edmunds et al., 2001).

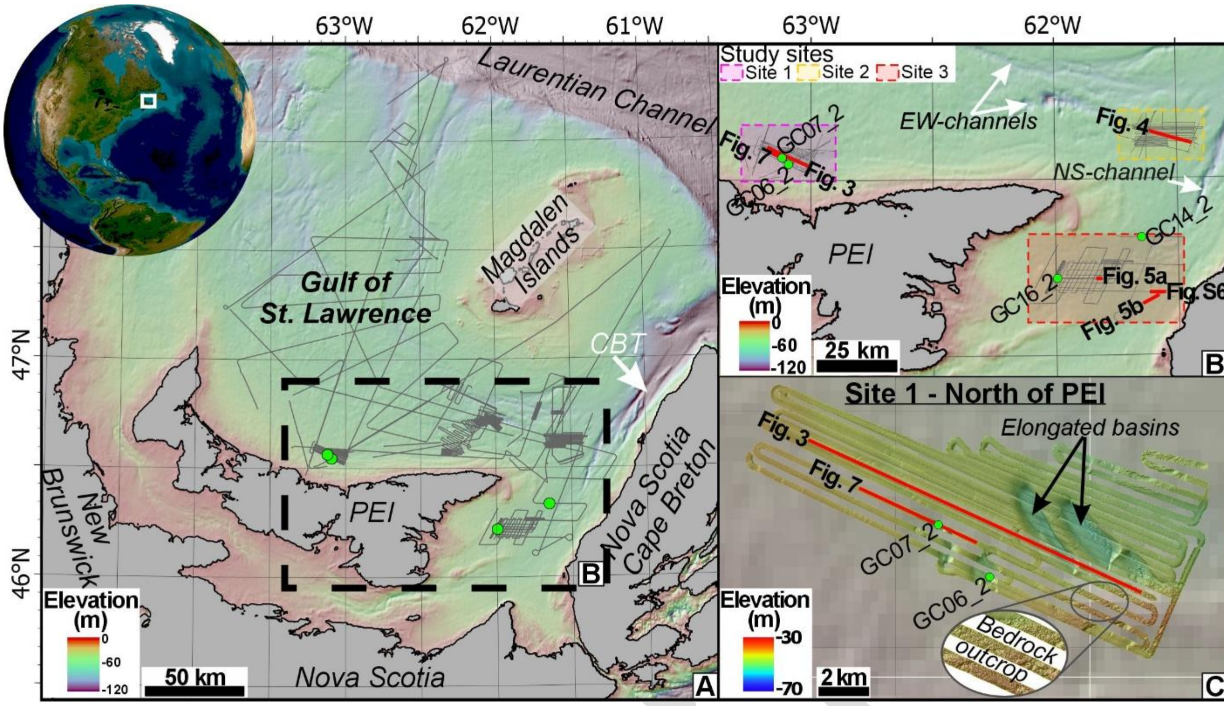

Fig. 1: A) Overview of the study area in the southern Gulf of St. Lawrence; B) zoom to study sites that are located north (Site 1, pink box), northeast (Site 2, yellow box) and east (Site 3, red box) of PEI; and C) multibeam bathymetry map of Site 1. Grey lines are the sub-bottom profiles acquired during MSM103 with the ones used in this study shown in B), while the red lines are the profiles presented in the figures. Green dots show the location of sediment cores selected for this study. Morphologically significant sites and special characteristics are highlighted. CBT stands for Cape Breton Trough. The maps were generated using ArcGIS pro and background bathymetric data were downloaded from GEBCO.

2. Regional Geology

The southern Gulf of St. Lawrence is a semi-enclosed basin of ~61,500 km^2 located on the Eastern Canadian continental shelf. It is bordered to the west by New Brunswick, to the south by PEI and Nova Scotia, respectively, to the east by Cape Breton Island of Nova Scotia, and to the north by the Laurentian Channel (Fig. 1a). The shelf generally shows a rugged or uneven terrain with numerous 100 to 200 m deep topographic depressions such as the Cape Breton Trough (CBT), which is located in its eastern portion (Figs. 1a & b) (e.g., Loring & Nota, 1973). Most of the channels are NE-oriented towards the Laurentian Channel. EW-trending channel systems that are 70 to 80 m deep are present between PEI and the Magdalen Islands towards the CBT (Figs. 1a & b).

The region is part of the Maritime Basin, which is filled with Devonian to Permian terrigenous fluvio-deltaic and shallow-marine sandstones and shales that were primarily deposited under arid and semi-arid conditions (Carr, 1969; Van de Poll, 1989; Symons,1990; Gibling et al., 2019). These strata are widely known as the PEI gray- and red-beds due to their distinctive color and exposure throughout the island (Carr, 1969, Van de Poll, 1989). Based on deep seismic profiles and exploration wells the basin fill is distinguished into four megacycle sequences, known as Bradelle, Green Gable, Cable Head and Naufrage Formation, which have different grain sizes and compositions (Van de Poll, 1989; Symons,1990; Gibling et al., 2019). An "unnamed Permian sandstone" present within wells forms the top of the megacycles (Gibling et al., 2019). The Paleozoic rocks are directly covered Quaternary sediments (Carr, 1969; Loring & Nota, 1973; Jiang & Somers, 2009).

The Pleistocene glaciations, and particularly the last one, significantly altered the preglacial landscape (Loring & Nota, 1973). At the climax of the LGM, the LIS extended across North America to the edge of the Eastern Canadian continental shelf (Shaw et al., 2006; Stea & Mott, 1989; Stea, 2011). An increase in global temperatures at ~16 ka BP led to thinning of the ice mass across PEI and Nova Scotia, and resulted in major calving episodes with massive ice streams through the Laurentian Channel (Shaw et al., 2006; 2009; Stea, 2011). The ice retreated rapidly from the Gulf of St. Lawrence and by 13 ka BP most of the ice mass was primarily onshore in the form of localized ice centers (Stea & Mott, 1989; Shaw et al., 2006; 2009; Stea, 2011), with one located on PEI (Loring & Nota, 1973, Vacchi et al., 2018). It is suggested that the Younger Dryas cooling event resulted in a re-advance of the isolated marine and terrestrial ice remnants and potential formation of new ice caps (Stea & Mott, 1989; Shaw et al., 2006, Stea, 2011, Vacchi et al., 2018). Global warming after the Younger Dryas led to a complete removal of the ice mass from the Gulf of St. Lawrence by 10 ka BP (Vacchi et al., 2018).

Each ice retreat and re-advance was likely accompanied by marine transgressions and regressions, driven by a combination of eustatic changes and local tectonic movements (Fairbanks, 1989; Person et al., 2003; Forbes et al., 2014). Previous studies suggested that the Gulf of St. Lawrence was rapidly flooded between 16 and 12 ka BP (Forbes et al., 2004; 2014; Loring & Nota, 1973), and that isostatic rebound between 10 and 9 ka BP caused an uplift of the entire region and consequently a drop in RSL of several tens of meters, resulting in the subaerial exposure of part of the continental shelf (Forbes et al., 2004; 2014; Shaw, 2005; Vacchi et al., 2018). RSL rose following this lowstand, as a collapse of the forebulge margin and hydro-isostatic loading caused tectonic subsidence (Forbes et al., 2004; 2014). From 6 ka BP, this subsidence is less pronounced but continues to this day (Forbes et al., 2004; 2014).

3. Methods

This study focuses on three study sites with the highest data density, which are located north, northeast and east of PEI, and termed Site 1, 2 and 3 respectively (Fig. 1b). All geophysical and sedimentological data were collected during the 60-day-long research expedition MSM103 in 2021 onboard of the R/V Maria S. Merian (Hölz, 2022).

3.1. Hydroacoustic data sets

3.1.1. Multibeam echosounder data

Multibeam echosounder data were acquired using the Kongsberg Simrad EM712 system. This system operates at a nominal frequency of 40 to 100 kHz and allows data acquisition between 5 and 3,600 m water depth (mwd) (Kongsberg, 2022). Bathymetric data were processed using the open access software MB-System (version 5.8.1), gridded at 2 m resolution, and used for geomorphological characterization.

3.1.2. Sub-bottom profiles

Sub-bottom profiles were acquired using the Atlas Parasound P70 acquisition system. This parametric echo-sounder operates at 4 kHz. In the Gulf of St. Lawrence, the imaging depth is 10 to 45 m depending on the sediment thickness, composition and presence of gas-charged sediments. The data have a vertical resolution of 0.15 m calculated considering a sound velocity of 1,500 m s^{-1} and a minimum horizontal resolution of 3.5 to 14 m between 50 to 200 mwd (Spieß, 1993; Teledyne Marine, 2017). Further specifications on data acquisition during MSM103 are provided in the cruise report (Hölz, 2022). The software Kingdom Suite^{TM} (UTM zone: 20N) was used to analyze the sub-bottom profiles and generate surface maps of key reflection horizons needed for paleo-morphological reconstructions and to understand the role of sediment transport, deposition, and erosion in the study sites. For both seismic profiles and maps the depth is in two-way travel time (ms) from sea level.

3.2. Sediment analysis

Eight gravity cores, 0.66 to 4.62 m in length, were collected north, northeast and east of PEI and were split, lithologically described, and sampled onboard (Hölz, 2022). Four sediment cores, GC06_2, GC07_2, GC14_2 and GC16_2 located within Sites 1 and 3 (Fig. 1b), were further sampled for grain size analysis, radiocarbon dating and foraminifera extraction needed for environmental reconstructions. No sediment core was available directly from within Site 2 (Fig. 1b).

3.2.1. Grain size

Samples for grain size analysis were extracted every 10 cm from the four sediment cores (GC06_2. GC07_2, GC14_2, GC16_2). The 148 sediment samples were treated with 50 ml of hydrogen peroxide (H_2O_2) to remove organic components and dispersed with a Hydro EV unit before being analyzed with a Mastersizer Malvern 3000 at the University of Modena and Reggio Emilia.

3.2.2. Age control

Twenty samples consisting of whole shells, mixtures of benthic and planktonic foraminifera, as well as wood and plant remains were extracted for AMS Radiocarbon dating at the Póznan Radiocarbon Laboratory. The open access software OxCal version 4.4 was used to calibrate the measured ^{14}C values (Ramsey, 2009). A regional correction factor (ΔR -83±50) was applied for the Gulf of St. Lawrence (McNeely et al., 2006). Given the differences in the dating material, two separate calibration curves - terrestrial (IntCal20, Reimer et al., 2020) and marine (marine20, Heaton et al., 2020) - were used for the calibration. The calibrated ages are reported in calendar age Before Present (cal a BP) with a 2-sigma range to constrain the age model and are correlated to sub-bottom profiles.

3.2.3. Foraminifera analysis and paleo-environmental reconstruction

Fifteen, 1-cm-thick sediment samples were collected from the cores GC06_2, GC07_2, GC14_2, GC16_2. The samples were dried at 50°C and washed through a 0.063 mm mesh sieve. The relatively high amount of fine sand in the washed fraction strongly diluted the foraminifera specimens, and therefore the washed samples were further sieved with 0.106 mm and 0.125 mm meshes. The fraction >0.125 mm was examined for foraminifera analysis, and the fraction between 0.106 and 0.125 mm was checked for the presence of taxa with elongated shape (e.g., *Fursenkoina*) or small adult specimens. A semiquantitative analysis at species level was carried out. The taxonomy is based on Brady (1884), Vilks (1969, 1989), Hansen and Lykke-Andersen (1976), Scott et al. (1977, 1980), Schafer and Cole (1982), Vilks et al. (1982), Schröder-Adams et al. (1990), Thomas et al. (1990), Scott and Vilks (1991), Jennings and Helgadottir (1994), Cage et al. (2021) and the nomenclature updated according to Hayward et al. (2025) (see Table S1 for details). The main taxa are illustrated in Supplementary Material Plate I and II.

4. Results

4.1. Geomorphology of the study sites

Site 1 is located ~14 km north of PEI in 40 to 50 mwd (Figs. 1b & c). The seafloor topography is generally smooth and almost flat within an otherwise rugged seafloor terrain, which can be observed in the northern and southern portions of this site (Fig. 1c). Up to 7 m deep, NW- to SE-oriented depressions are evident across the central to eastern portions of Site 1 (Fig. 1c). Site 2 is located ~30 km northeast of PEI at 60 to 70 mwd, and 10 km south of the EW-trending channel systems present between PEI and the Magdalen Islands (Figs. 1a & b, S1). The seafloor at this site shows an overall smooth and flat topography, except for some wavy features that are located in the northwestern portion (Fig. S1). Site 3 is located ~25 km to the east of PEI at 45 to 60 mwd (Fig. 1b), and the seafloor comprises a mix of rugged and smooth topography (Figs. 1b, S2). A NE-oriented channel system is noticeable to the east of Site 3 in proximity to Cape Breton, and leads towards Site 2 and the CBT (Figs. 1a & b).

4.2. Seismic stratigraphy

Six major reflection horizons (R1 to R5) plus the seafloor (Sf), and six acoustic units (U0 to U5) were identified based on their distinct reflection characteristics and mapped along the three study sites (Fig. 2, Table 1). The reflection horizons generally confine the units on either the top or bottom, except for R6, which is a characteristic internal reflection within U5 (Fig. 2, Table 1).

Table 1: Units and acoustic facies identified in the three study sites (Site 1, 2 and 3).

Unit	Examples		Description
Unit 5 (U5)	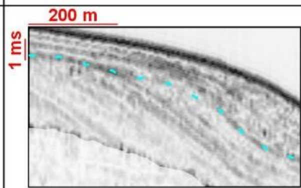	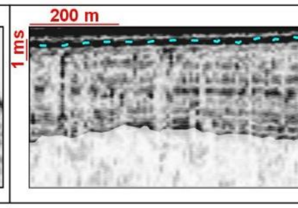	Distinct, coherent to incoherent, parallel and at times intermittent sub-bottom reflections; separated by a erosional truncation (blue dots) into an upper (U5-a) and lower (U5-b) unit (1.5-9 ms-thick).
Unit 4 (U4)	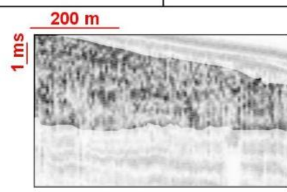		Incoherent internal reflections with at times indistinct, intermittent, parallel sub-bottom reflections (0.5-6 ms-thick).
Unit 3 (U3)	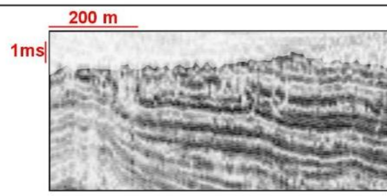		Distinct, coherent, parallel, generally high amplitude sub-bottom reflections; at times intermittent, indistinct reflections (2.5-36 ms-thick).
Unit 2 (U2)	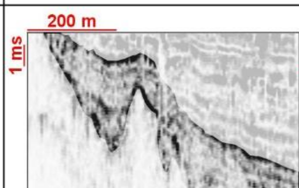	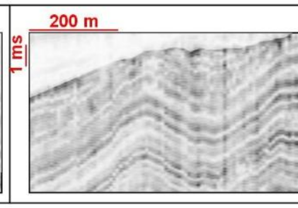	Distinct, coherent, parallel sub-bottom reflections at times intermittent; generally low amplitude, locally higher amplitudes; conform to U1 and variable in thickness (1.5-13 ms-thick).
Unit 1 (U1)	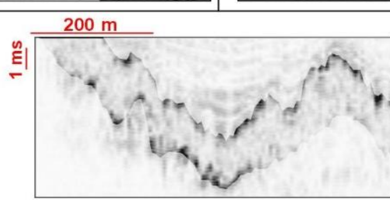		No apparent sub-bottom reflections (transparent); at times with incoherent, high amplitude internal character; often appears irregular/hummocky (2.5-12 ms-thick).
Unit 0 (U0)	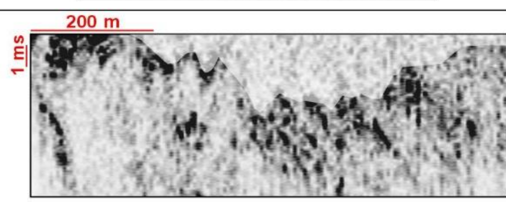		No sub-bottom reflections or high amplitude, incoherent, often gentle dipping sub-bottom reflections.

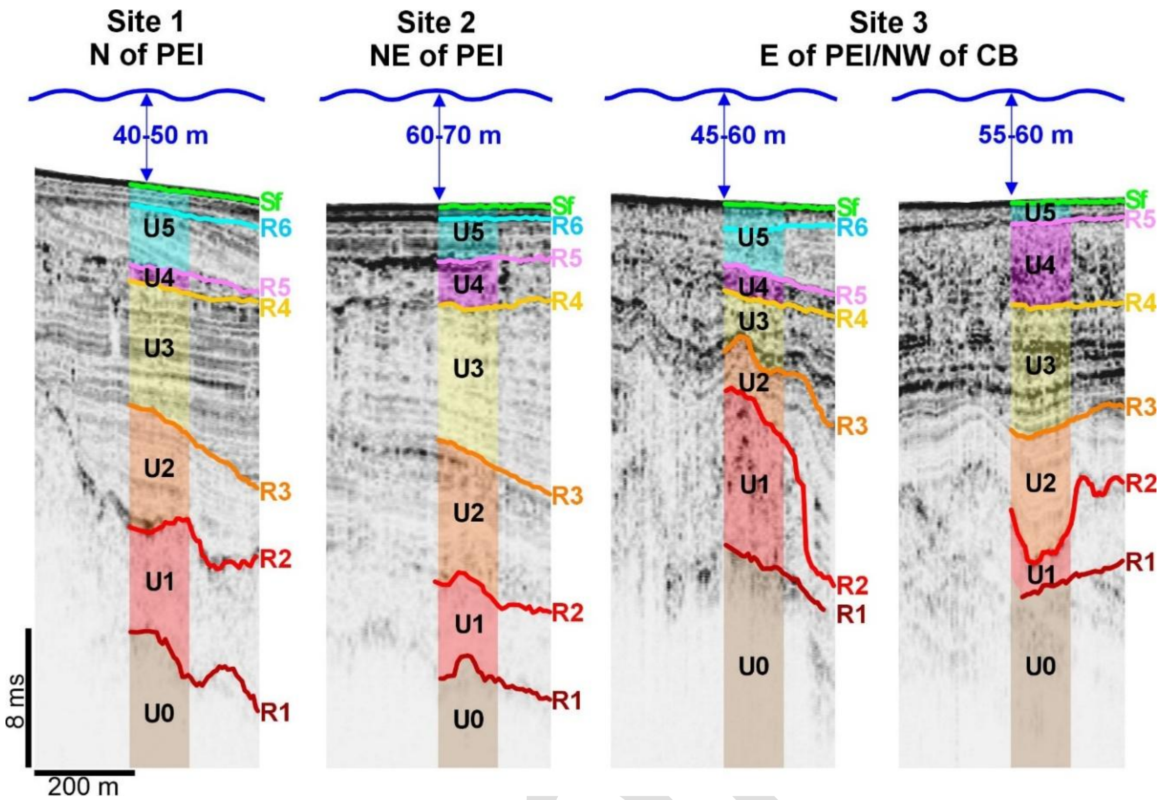

Fig. 2: Comparison of key acoustic reflections (R1-R6) and units (U0-U5) that were identified and mapped together with the seafloor reflection (Sf) within the three study sites (Site 1, 2 and 3). The reflections (R1-R6) are highlighted to the right, and acoustic units (U0-U5) are shown within the different colored boxes. All profiles have the same scale. The average water depth for each site is shown on top of each panel. Note that due to its size, we decided to show two examples for Site 3, which represent opposite shores lines being located <20 km from the coasts of PEI and Cape Breton.

4.2.1. Unit U0

In the three study sites, unit U0 is found underneath and besides the buried depressions and is characterized by no sub-bottom reflections or high amplitude incoherent, often dipping sub-bottom reflections (Fig. 2). Limitations in the acoustic penetration does not allow to image the base of U0.

4.2.2. Horizon R1 and Unit U1

R1 is the lowermost mappable horizon imaged in sub-bottom profiles crossing the buried depressions (<30 m deep, e.g., Site 1 & 3) (Fig. 2). It is a high amplitude reflection that is often incoherent and locally not visible due to the limited acoustic penetration depth of the sub-bottom profiles (e.g., depressions within Site 2; >45 m deep) (Figs. 3, 4). Unit U1 on top of horizon R1 varies in thickness between 2 and 9 m (Fig. 3, Table 1). This unit is generally transparent with no apparent sub-bottom reflections (Figs. 2, 3, 4; Table 1). At times, single incoherent, high amplitude reflections are noticeable within U1, especially in sub-bottom profiles from Site 2 (Fig. 4).

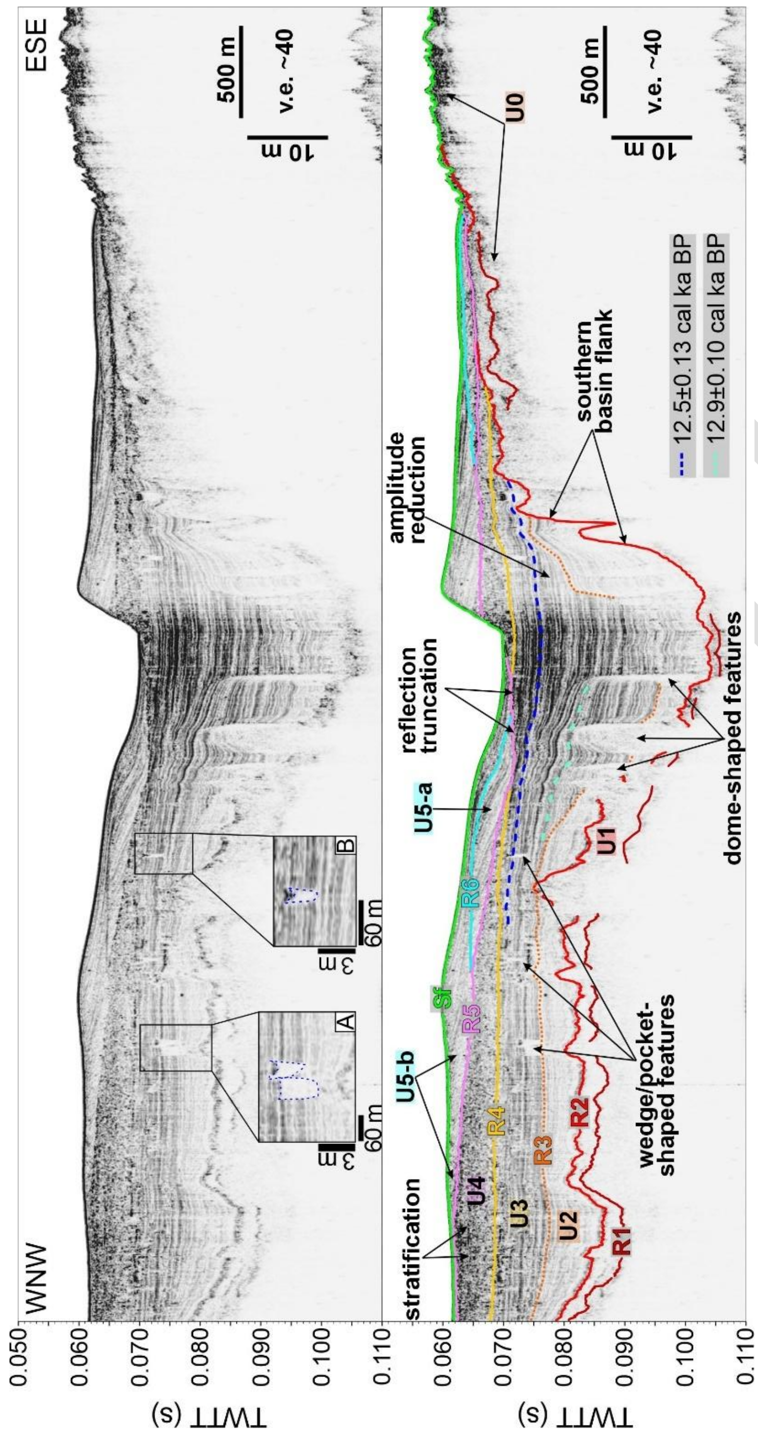

Fig. 3: WNW to ESE oriented sub-bottom profile acquired north of PEI (Site 1; see location in Fig. 1b). The top image shows the uninterpreted profile, while the bottom image shows the interpretation. Insets A) and B) in the to image

show wedge-shaped features and pockets (blue dashed relief) that occur within U3. The distribution of key reflection horizons (R1-R6), acoustic units (U0-U5) and important reflection characteristics are highlighted. Radiocarbon ages from core GC07_2 are correlated to this profile (dashed blue and turquoise lines).

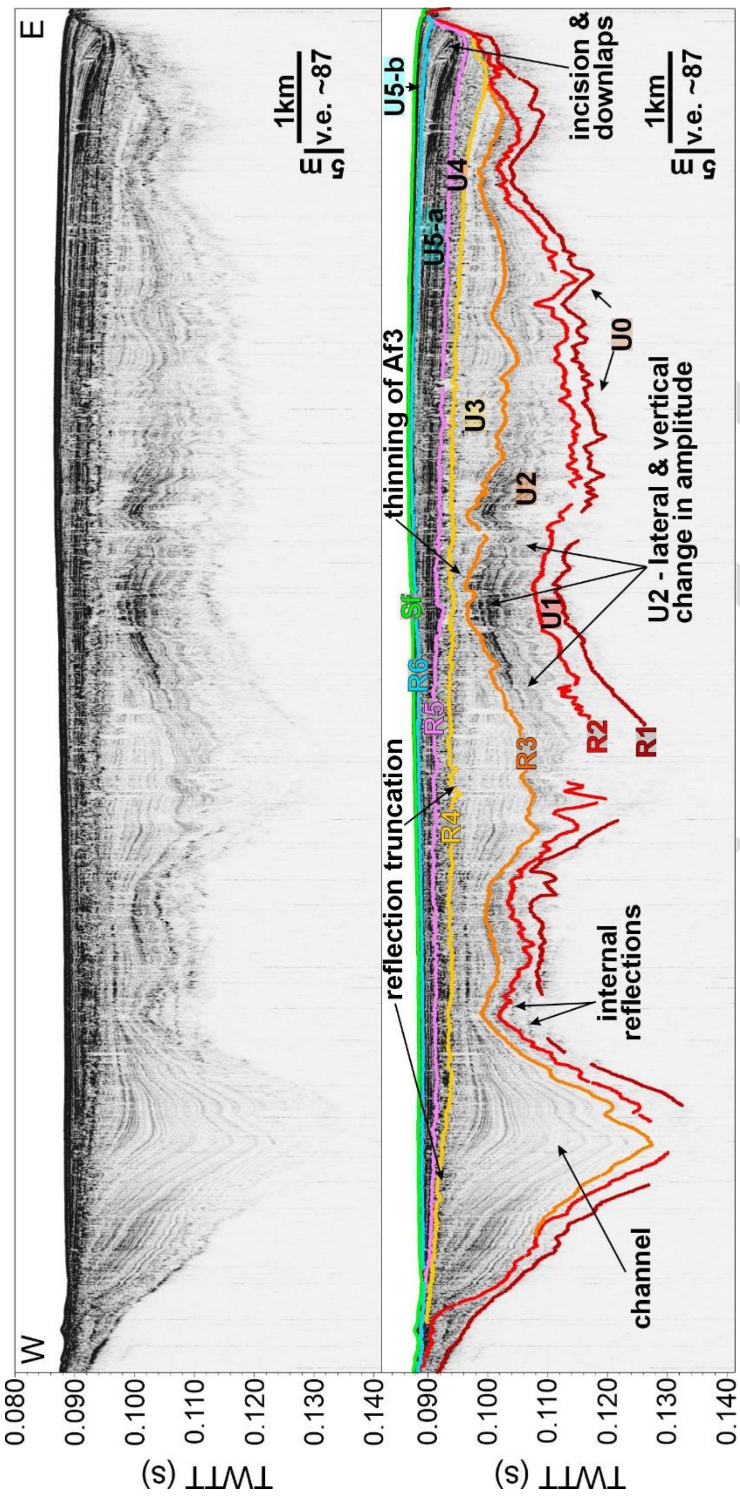

Fig. 4: W to E oriented sub-bottom profile acquired northeast of PEI (Site 2; see location in Fig. 1b). The top image shows the uninterpreted profile, while the bottom image shows the interpretation. The distribution of key reflection horizons (R1-R6), acoustic units (U0-U5) and important reflection characteristics are highlighted.

4.2.3. Horizon R2 and Unit U2

R2 is present within all sub-bottom profiles and is the lower reflection of a high-amplitude, coherent, hummocky double reflection on top of U1 (Fig. 2). This horizon is mostly conformable to R1, except where U1 shows a larger increase in thickness (Figs. 2, 4, 5a). Both horizons R1 and R2 form topographic heights within the sub-bottom depressions (Figs. 3, 5a & b). Unit U2 is found on top of R2 and varies in thickness between 1 and 10 m (Figs. 2, 4, 5a; Table 1). It shows coherent, generally low amplitude, stratified reflections that are conformable to horizon R2 (Figs. 2, 3, 4, 5a). U2 is primarily present within deeper depressions and can be locally absent, especially within Sites 1 and 3 (Figs. 3, 5a & b). In Site 2, a change in amplitude of U2 is noticeable with higher reflection amplitudes being present along the sides of deeper depressions (Fig. 4; Table 1). These higher reflection amplitudes intertwine with and partly overly the lower amplitude reflections of this unit (Fig. 4). U2 and the overlying Unit U3 have similar reflection characteristics, but different reflection amplitudes (Fig. 2; Table 1).

289 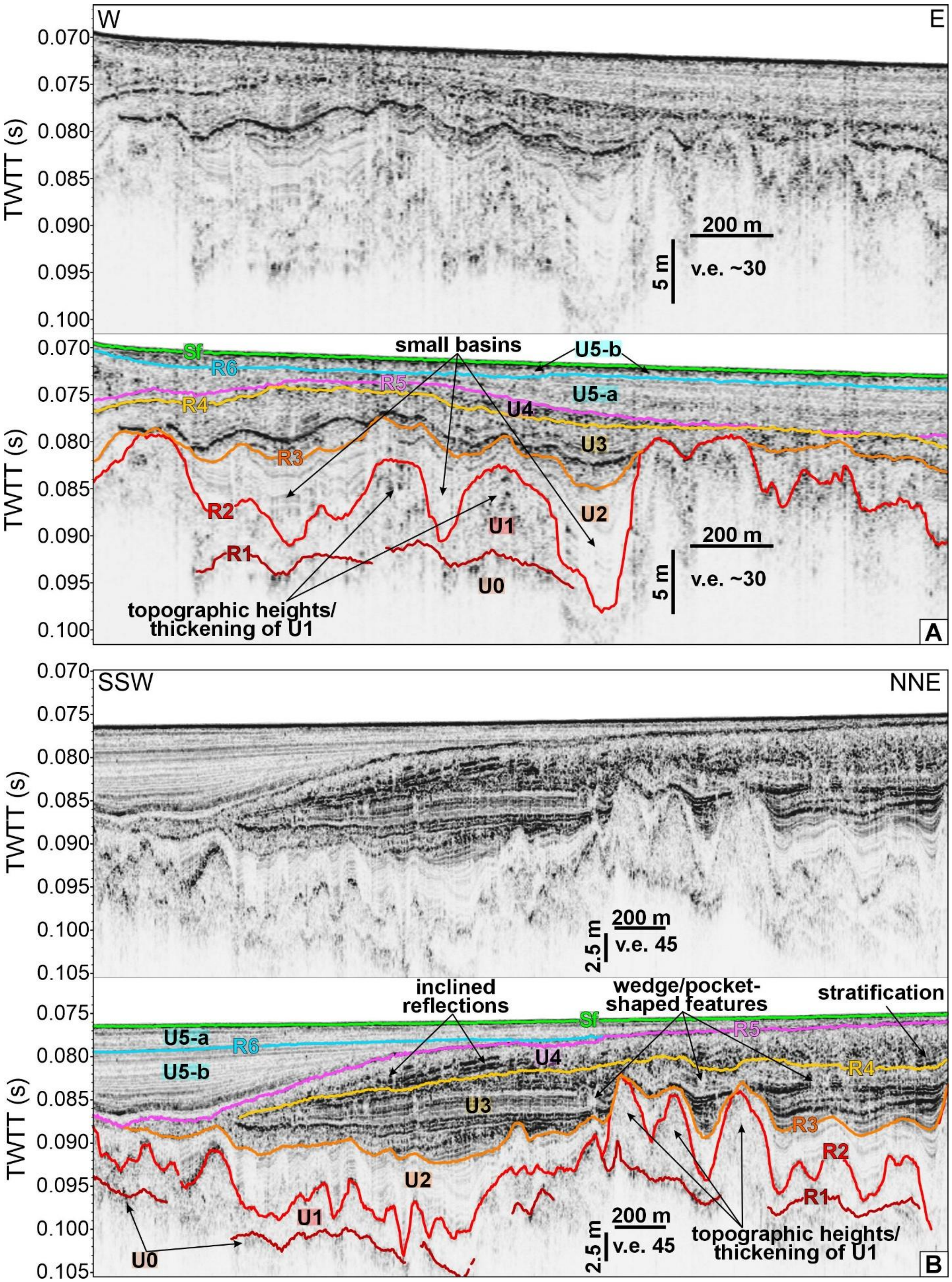

W
E
TWTT (s)
200 m
5 m
v.e. ~30
Sf
R6
R5
R4
R3
R2
R1
U5-b
U5-a
U4
U3
U2
U1
U0
small basins
topographic heights/
thickening of U1
A
SSW
NNE
200 m
2.5 m
v.e. 45
inclined
reflections
wedge/pocket-
shaped features
stratification
topographic heights/
thickening of U1
B

Fig. 5: A) W to E oriented sub-bottom profile acquired ~40 km offshore, east of PEI; and B) an SSW to NNE oriented sub-bottom profile acquired ~12 km off Cape Breton. In both cases, the top image shows the uninterpreted profile, while the bottom image shows the interpretation. The distribution of key reflection horizons (R1-R6) and acoustic units (U0-U5) as well as important reflection characteristics are highlighted. The location of the profiles is shown in Fig. 1b.

4.2.4. Horizon R3 and Unit U3

R3 highlights the transition from U2 into U3 (Figs. 3, 4, 5a & b). This horizon is overall conformable to the underlying reflections of U2, but locally truncates U2 reflections, particularly within Site 2 (Figs. 3, 4; Table 1). R3 is often a coherent, high amplitude reflection in Site 2 and 3, but it is partially absent, especially within Site 1 where R3 does not form a coherent reflection (Figs. 2, 3, 4, 5a & b). U3 is located on top of R3 and overall, 2 to 12 m thick, except for Site 2 where it is up to 25 m thick (Figs. 2; 4, Table 1). This unit shows high amplitude, coherent and in part intermittent, stratified reflections, which contrast with the generally low amplitude reflections of U2 (Fig. 2; Table 1). U3 reflections, which are often unconformable to U2 reflections, onlap horizon R3 (Fig. 2). Low amplitude to transparent, wedge-shaped features, and pockets are noticeable within U3, especially towards its top (Figs. 3, 7). Distinct reflections are visible below these features (Fig. 7). Within Site 1, we further observe dome-shaped features with low amplitude to no sub-bottom reflections within U2 and U3 (Fig. 3).

4.2.5. Horizon R4 and Unit U4

R4 forms the top of U3 and base of unit U4 (Fig. 2). This horizon forms an erosional truncation to U3 reflections, especially within Site 1 and 2, but locally also appears conformable to the underlying reflections (Figs. 2, 3, 4; Table 1). The overlying unit U4 is of variable thickness in the range of 0.3 to 4.5 m (Figs. 2, 3). U4 shows primarily chaotic, high amplitude reflections with at times interbedded stratified, parallel reflections (Figs. 2, 3, 4; Table 1). In proximity to Cape Breton (Site 3), stratified reflections of U4 are more abundant, but a seaward inclination and onlap horizon R4 is evident (Fig. 5b).

4.2.6. Horizon R5 and R6 and Unit U5

R5 forms the top of U4 (Fig. 2) and generally appears wavy due to the variations in thickness of the underlying unit (Figs. 3, 5b). Unit U5 is located on top of R5 and is on average 1 m thick in

Site 1 and up to 7 m thick in Site 2 and 3. This unit consists of distinct, coherent and occasionally incoherent, parallel sub-bottom reflections (Fig. 2; Table 1). It can be subdivided into a lower (U5-a) and upper (U5-b) portion, which is separated by an internal high amplitude, often unconformable reflection named horizon R6 (Fig. 2; Table 1). The lower portion of U5 (U5-a) below R6 is usually >1 m thick. It is, however, almost absent in Site 1, except for within the elongated seafloor depressions, where U5-a shows reflection downlaps (Fig. 3). In Site 2, U5-a reflection downlaps are associated with local, anticlinal unconformities and are associated with various channel incisions (Fig. 4). The upper portion of U5 (U5-b) on top of R6 is more widely distributed than U5-a and usually forms a <1 m thick layer on top of U5-a or on top of U4 if U5-a is absent (Figs. 3, 4, 5b). Within elongated depressions of Site 1, U5-b shows reflection downlaps like U5-a, but they are more gently inclined than those in U5-a (Fig. 3). Acoustic blank pockets and wedge-shaped features are found within U5, but only in Site 2, and in contrast to those observed within U3, vertical, linear acoustic blanking is apparent underneath these features (Fig. 4, 5a).

4.3. Reconstruction of paleosurfaces

Surface maps of reflection horizons, R1, R2, R4 and R5 provide insights into erosional and depositional changes within the study sites. R3 was not mappable for this purpose due to its partial absence, especially in Site 1. In addition, a surface grid of horizon R4 for Site 3 was not feasible, due to problems correlating between the widespread depressions that are separated by bedrock outcrops. Main morphological differences observed within each study site are presented in the following sections.

4.3.1. Morphological evolution of Site 1

Grids of horizons R1 and R2 reveal the presence of two, 15 to 30 m deep depressions resembling basins: a larger one (~29 km^2, basin 1) in the center of the study site and a small one (~4.5 km^2, basin 2) in its western portion (Fig. 6a). Basin 1 appears slightly elongated parallel to the present-day coastline of PEI (Fig. 6a). A noticeable 1 km wide, 8 km long and up to 35 m deep depression (7.4 km^2) is evident within basin 1 and extends parallel to its southern flank (Figs. 3, 6a). In contrast to horizons R1 and R2, R4 shows an almost flat, seaward inclined topography, as both basins have been filled with U2 and U3 material (Figs. 3, 6b). At horizon R5, several NNW-SSE-oriented, 3.5

to 14 m deep, 0.8 to 1.3 km wide and 0.8 to 3.5 km long depressions are present in the central to eastern portions of the study site (Fig. S3). Most of these depressions are still observable along the present seafloor but are reduced to about half their size with their center being shifted northward after infill with U5 material (Fig. S3).

4.3.2. Morphological evolution of Site 2

Surface maps of horizons R1 and R2 show three elongated NE- and EW-trending depressions that resemble channels (Figs. 4; 6c). The main system extends from the southwestern portion of Site 2, termed 'southern flank', NE-ward and bifurcates into two, parallel extending NE-trending elongated depressions (Fig. 6c). An EW-trending elongated depression is also observed in the northern part of Site 2, which leads into the main, NE-ward oriented system of this site (Fig. 6c). The depressions at R1 are ~1.8 km wide with an incision depth between 10 and 30 m (Fig. 6c). At R2 their width is reduced to ~1.4 km but with a similar incision depth (up to 30 m) (Fig. S4). The NE-trending elongated depressions disappear at R4, while the EW-trending elongated depression is still present but notably reduced in width and depth e.g., from a width of 1.9 km with a depth of 15 to 25 m at horizon R2 to a width of 0.9 km and depth of 5 to 10 m at horizon R4 (Fig. 6d). Like in Site 1, R4 appears slightly inclined seaward (Fig. 6d). The present seafloor shows no depressions or channels in Site 2, but EW-trending seafloor channels are present north of Site 2 (Figs. 1b, S1, S4).

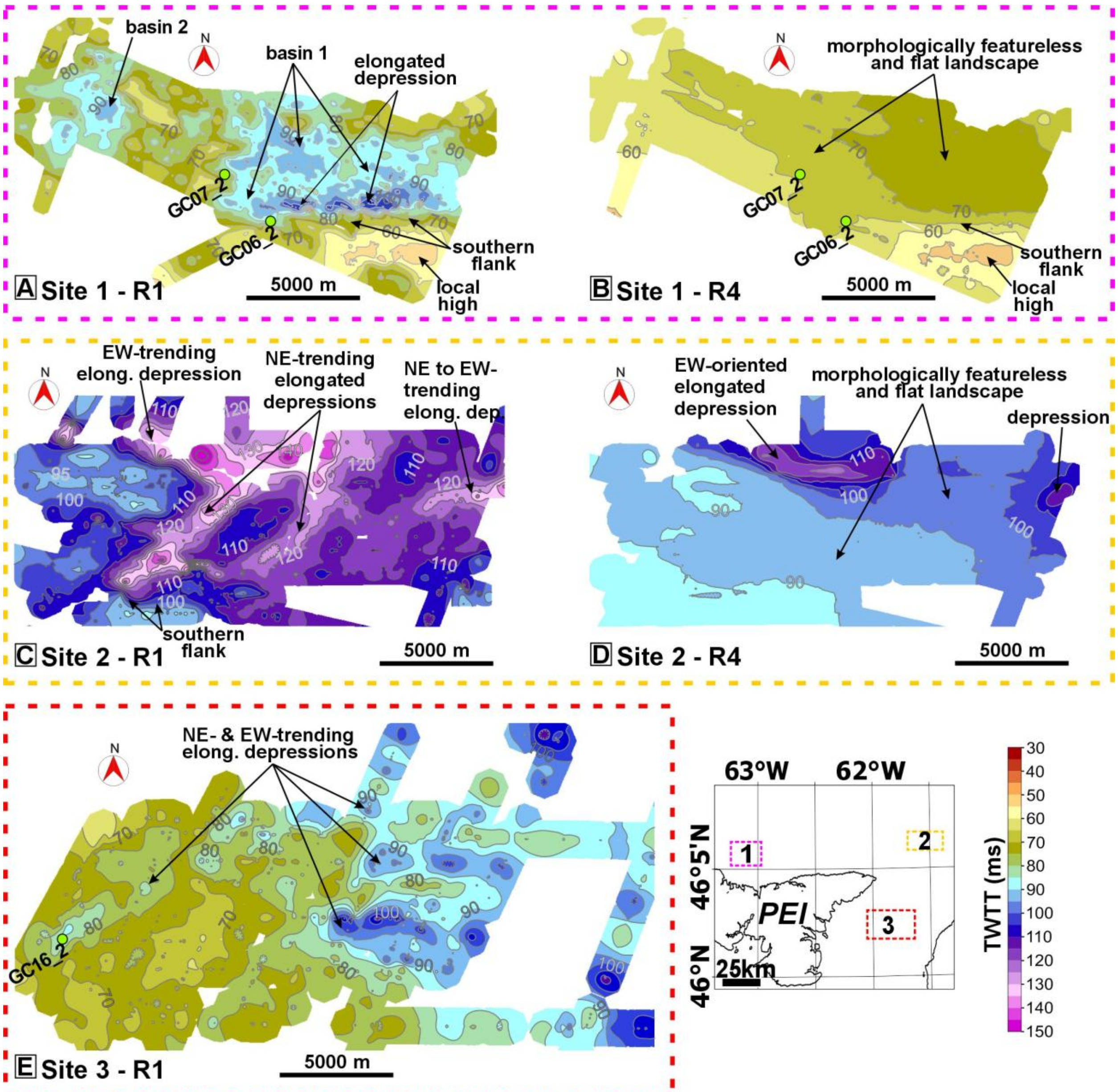

Fig. 6: Comparison of surface grids from the three study sites (Site 1, 2 & 3) along the Gulf of St. Lawrence showing the distribution of horizon R1 and R4 mapped using sub-bottom profiles. Surface grids of horizon R1 and R4 are shown for Site 1 in panel A) and B) (pink box), Site 2 in panel C) and D) (yellow box), and of horizon R1 for Site 3 in panel E) (red box). The overview map in the lower right corner shows the location of the three sites (dotted boxes 1, 2 & 3). Light green circles with black outlines show the location of sediment cores (GC06_2, GC07_2; GC16_2).

4.3.3. Morphological evolution of Site 3

Similar to Site 2, numerous NE to EW-trending, elongated depressions are present along horizons R1 and R2 (Fig. 6e). These horizons occur in 50 to 60 mwd with 4 to 25 m deep incisions (Fig.

6e). The EW-trending depressions extend from the coast of PEI and widen offshore where they are up to 2.8 km wide (Fig. 6e). The largest elongated depression is NS-trending, up to 35 m deep and 6 km wide, and located proximally to Cape Breton (Fig. 6e). The depressions are still visible at horizon R2 but are reduced in size and the incision is shifted further offshore away from PEI (Fig. S5). From horizon R2 to the modern seafloor the depressions diminish in size and their incision is shifted further offshore (Figs. S2, S5). No depressions or channels are visible along the modern seafloor east of PEI, as these are located further east and northeast of PEI (Figs. 1b, S2, S5).

4.4. Description of sediment cores

4.4.1. Sedimentological characteristics

4.4.1.1. Site 1

Two sediment cores (GC06_2, GC07_2) were collected within elongated seafloor depression where U4 and U5 are either absent or <30 cm thick (Fig. 1b, 7). GC06_2 was retrieved from 49 mwd and is 3 m long, while GC07_2 was retrieved from 51 mwd and is 3.72 m long (Fig. 8). Between 3 to 0.2 m of GC06_2 and 3.72 to 0.22 m of GC07_2 both cores contain homogenous to massive dark reddish-brown to reddish-brown clay to clayey mud with traces of very fine to medium sand interbedded with layers of clay and silty sand (Fig. 8). Correlation of the cores to the sub-bottom profiles show that these sections of the cores (3-0.2 m of GC06_2, 3.72-0.22 m of GC07_2) sampled U3 (Fig. 7). In contrast, the upper 0.2 m of GC06_2 and 0.22 m of GC07_2 consist of homogenous, dark brown to dark reddish-brown, medium to coarse sand with small amounts of gravel that either originate from U4 or U5 (Figs. 7, 8). Both cores contain intact shells and shell fragments (Fig. 8).

4.4.1.2. Site 3

Two sediment cores were collected within Site 3. GC14_2 was retrieved from 60 mwd about ~40 km offshore PEI and is 4.62 m long, while GC16_2 was retrieved ~20 km from shore in 47 mwd and is 3.62 m long (Figs. 1, 8). GC14_2 consists of bioturbated, largely homogenous dark grayish brown to reddish-brown mud to silty mud and dark grayish brown sandy mud (Fig. 8). In contrast, GC16_2 contains bioturbated, homogenous dark grayish brown to reddish-brown sandy muds and silty muds with a higher amount of silt towards the top (Fig. 8). Correlations of GC14_2 and

GC16_2 to sub-bottom profiles show that these cores retrieved sediments from U5. Shells and shell fragments of various species are abundant within both cores. The deeper core sections contain higher amounts of organic material (wood or plant rests).

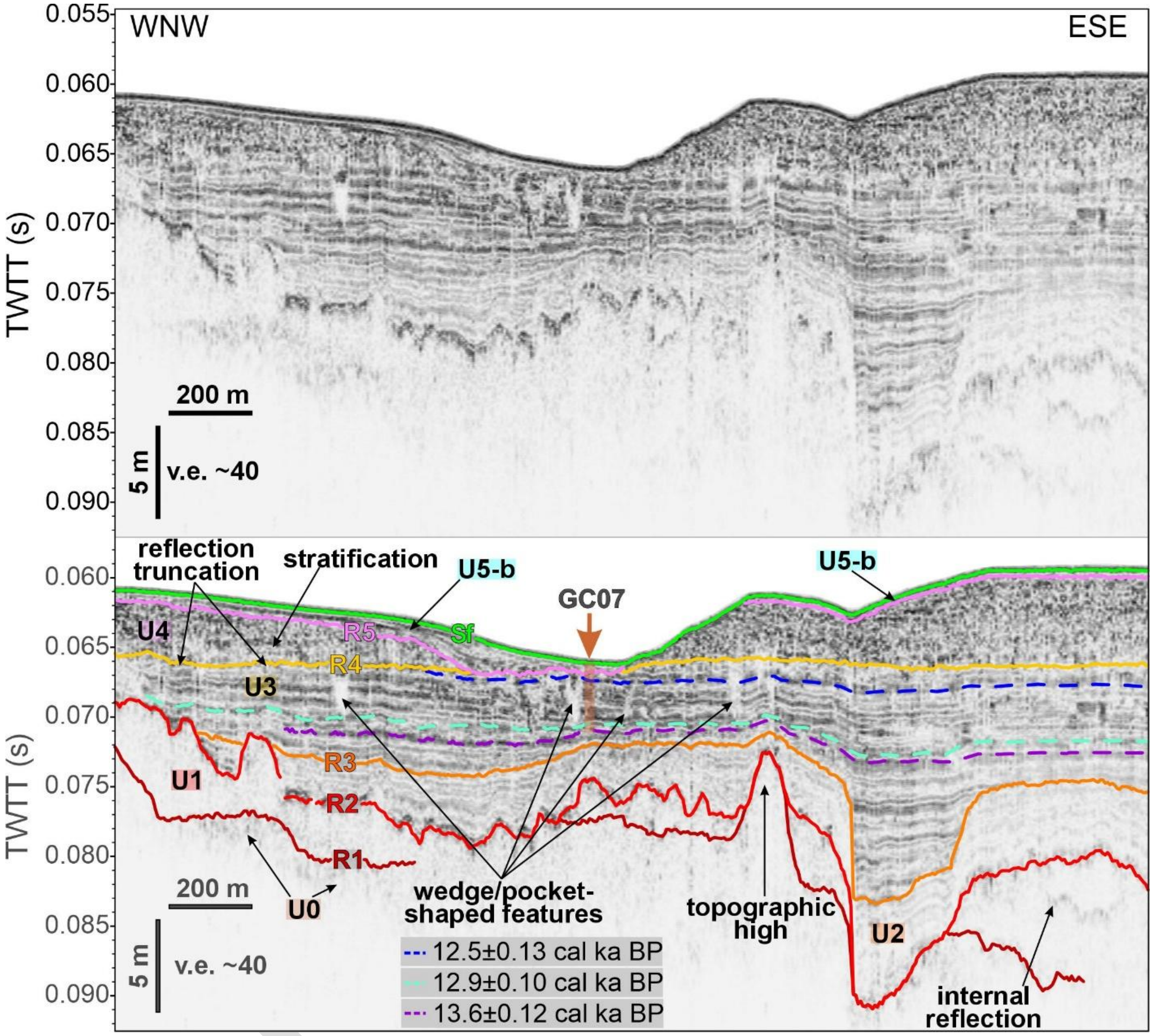

Fig. 7: Sub-bottom profile acquired north of PEI (Site 1, see location in Fig. 1b). The top image shows the uninterpreted profile, while the bottom image shows the interpretation with key reflection horizons (R1-R5) and acoustic units (U0-U5). Important reflection characteristics are highlighted. The location and depth of sediment core GC07_2 is shown (brown arrow and box), and the core stratigraphy was adopted into the sub-bottom profile (dashed blue, turquoise and lilac lines) with the corresponding age shown at the bottom of this figure. Note: horizon R6 is not shown as the lower portion of U5 (U5-a) is absent and its upper portion (U5-b) directly overlies U4.

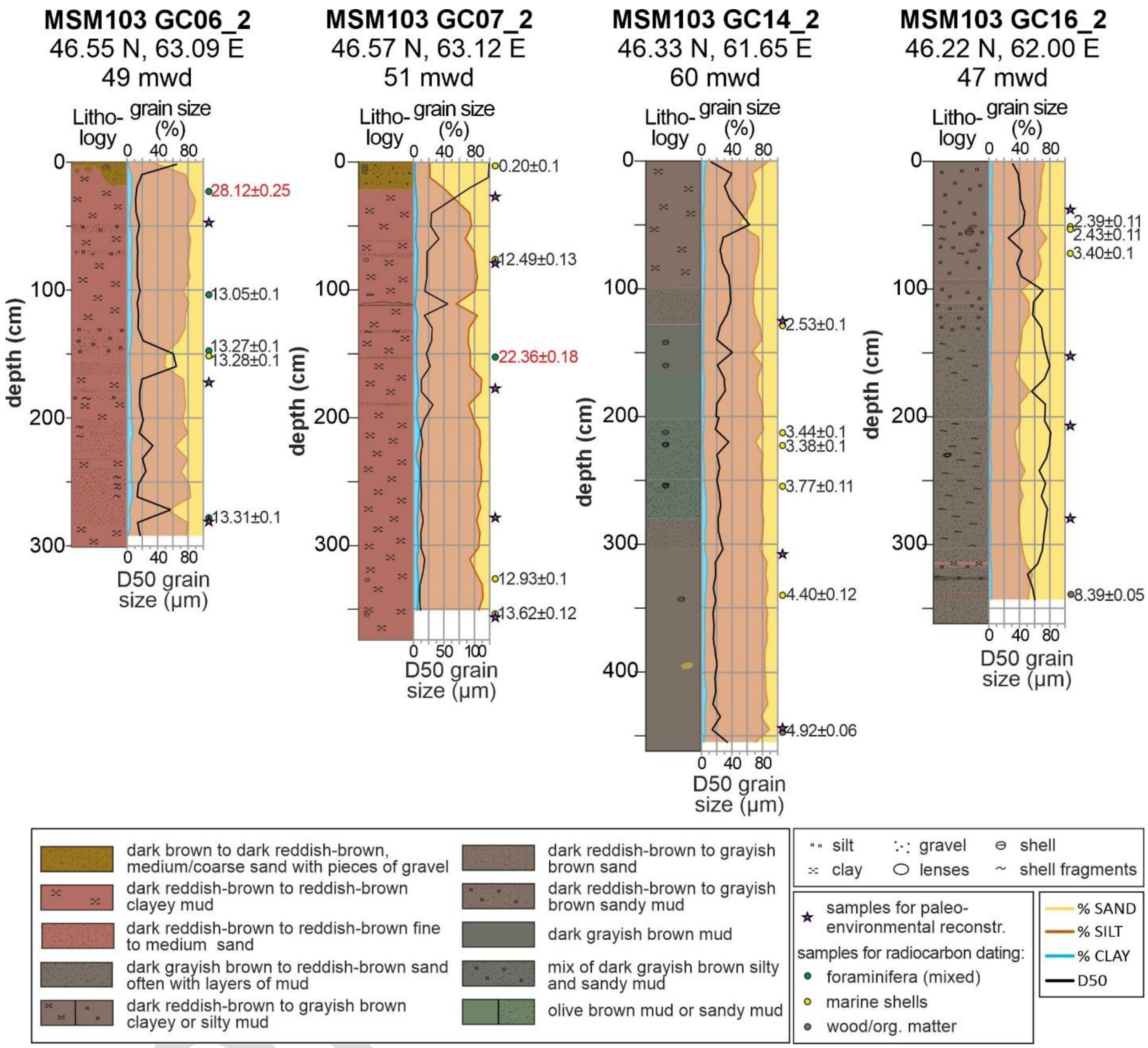

Fig. 8: Comparison of sediment core characteristics collected within the three study sites with GC06_2 and GC07_2 collected north (Site 1), and GC14_2 and GC16_2 collected east of PEI (Site 3). For each core the core lithology as well as measured percentage of clay, silt and sand, and median grain size (D50) in µm are shown. For details on the lithology see legend in the right corner; different colored dots next to the cores represent where samples for radiocarbon dating were extracted, while lilac stars show where samples for the biofacies analysis were extracted.

4.4.2. Biofacies description

The foraminiferal assemblages include only benthic foraminifera with a generally good preservation state (Table S1, Supplementary Plates I 6 II). Biofacies from all samples were described, even if there was a low foraminifera abundance. The foraminifera in the cores are distinguished into three different biofacies (A, B, C), which are indicative of different environments:

- Biofacies A is most common and was present within GC06_2, GC07_2, and in the lower part of GC16_2. This biofacies is dominated by the calcareous taxa *Elphidium excavatum* and *Elphidium clavatum*, along with by *Haynesina orbicularis* and *Buccella frigida.*
- Biofacies B only occurs in GC14_2 and is characterised by a generally poor assemblage, with *Nonionellina labradorica* and *Islandiella helenae* as relatively more frequent taxa, followed by *E. excavatum* and *E. clavatum.* Specimen tests occasionally show dissolution traces. Very rare specimens of the agglutinated taxa *Entzia macrescens, Lepidodeuterammina ochracea*, *Trochammina inflata* and *Trochammina squamata* are present, but given their very rare abundance we consider them as reworked.
- Biofacies C is only found in the upper part of GC16_2 and is largely dominated by agglutinated taxa, namely *Lagenammina difflugiformis*, followed by scattered specimens of *Lagenammina atlantica* and rare, or very rare, specimens of *E. excavatum* and *B. frigida*. The distinction between *L. atlantica* and *L. difflugiformis* can be challenging, but *L. atlantica* typically lacks a developed neck present in *L. difflugiformis* (cf. Todd and Low, 1981).

4.4.3. Geochronology and sedimentation rates

Of the 20 samples extracted for radiocarbon dating, two, GC06_2(a) and GC07_2(c), gave inverse ages suggesting that sediment was reworked and, therefore, were not considered for the age models and to calculate sedimentation rates (Table 2).

Sediment cores from Site 1 (GC06_2, GC07_2) that sampled U3 show calibrated ages from 13.6 to 12.5 ka cal BP, which correspond to the late Bølling-Allerød (13.6-12.9 ka cal BP) and early Younger Dryas (12.9-12.5 ka cal BP) (Figs. 8, 9; Table 2). The late Bølling-Allerød, which spans ~700 a, is ~0.75 m thick in the cores (GC06_2, GC07_2) and up to 1.12 m thick within basin 1 of Site 1 as shown by correlating the core stratigraphy to sub-bottom profiles (Figs. 3, 7). A sedimentation rate of ~0.1 to 0.16 cm a^{-1} can thus be estimated for the Bølling-Allerød. In comparison, the sediment portion corresponding to ~460 a of the Younger Dryas is 3 to 5.25 m thick within Site 1 (Figs. 3, 7), which implies a sedimentation rate of 0.62 to 1.08 cm a^{-1} for this period.

Sediment cores collected within Site 3 (GC14_2, GC16_2) are dated within the Holocene (11.6 ka BP to present) (Figs. 8, 9; Table 2). In all cases, the sampled sections correspond to U5 (Fig. 5a). For GC14_2 (Site 3), which is 4.5 m long and shows sediment ages within the late Holocene (5-2 ka cal BP), we can calculate sedimentation rates between 0.2 and 0.09 cm a^{-1} with a decrease towards the top of the core (Fig. 1b, 8). In comparison GC16_2 (Site 3, Fig. 1b), shows sedimentation rates between 0.07 and 0.05 cm a^{-1} for the past 8 ka. These findings show high sedimentation rates for the Bølling-Allerød and especially the Younger Dryas (0.1 to 1 cm a^{-1}) and smaller sedimentation rates during the Holocene (0.05 to 0.2 cm a^{-1}).

Table 2: Sediment samples and determined calibrated ages. Marked in red are dates that differ significantly from the other samples (above and below) and, therefore, were not considered further, such as for calculation of the sedimentation rates.

core name	sample name	depth (cm)	sample material	lab nr.	^{14}C a BP ± 1 σ	2 σ range cal. ages (cal a BP) (95 %)	average age (cal a BP)
GC06_2	a	23.0	foraminifera (mix)	Poz-171626	24,710 ± 190	28,598 - 27,695	**28,115 ± 240**
	b	104.0	foraminifera (mix)	Poz-171627	11,650 ± 60	13,269 - 12,839	**13,051 ± 106**
	c	148.0	foraminifera (mix)	Poz-171629	11,870 ± 60	13,481 - 13,085	**13,273 ± 103**
	d	152.0	marine shell	Poz-171630	11,880 ± 60	13,492 - 13,091	**13,283 ± 104**
	e	279.0	foraminifera (mix)	Poz-171631	11,910 ± 70	13,552 - 13,101	**13,314 ± 111**
GC07_2	a	3.0	marine shell	Poz-172453	665 ± 30	400 - 17	**201 ± 93**
	b	76.5	marine shell	Poz-171632	10,990 ± 50	12,660 - 12,180	**12,438 ± 128**
	c	153.0	foraminifera (mix)	Poz-171633	19,190 ± 120	22,740 - 22,034	**22,357 ± 175**
	d	327.0	marine shell	Poz-171634	11,520 ± 60	13,117 - 12,733	**12,925 ± 100**
	e	354.5	marine shell	Poz-171635	12,190 ± 60	13,876 - 13,390	**13,623 ± 118**
GC14_2	a	128.0	marine shell	Poz-171639	2,850 ± 30	2,724 - 2,344	**2,532 ± 103**
	b	213.0	marine shell	Poz-171640	3,610 ± 35	3,665 - 3,250	**3,444 ± 100**
	c	223.0	marine shell	Poz-171641	3,555 ± 30	3,574 - 3,189	**3,378 ± 97**
	d	255.0	marine shell	Poz-171689	3,875 ± 35	3,999 - 3,561	**3,772 ± 110**
	e	342.0	marine shell	Poz-171691	4,350 ± 35	4,642 - 4,179	**4,404 ± 115**
	f	448.0	wood fragment	Poz-172073	4,350 ± 40	5,040 - 4,841	**4,921 ± 59**
GC16_2	a	51.0	marine shell	Poz-171692	2,735 ± 35	2,638 - 2,176	**2,390 ± 113**
	b	53.0	marine shell	Poz-171693	2,765 ± 35	2,676 - 2,228	**2,429 ± 111**
	c	72.0	marine shell	Poz-171695	3,570 ± 35	3,606 - 3,209	**3,396 ± 100**
	d	399.5	org. sediment	Poz-172072	7,580 ± 50	8,519 - 8,212	**8,385 ± 52**
Indices:	Reservoir corr. marine samples: -83±50 a						

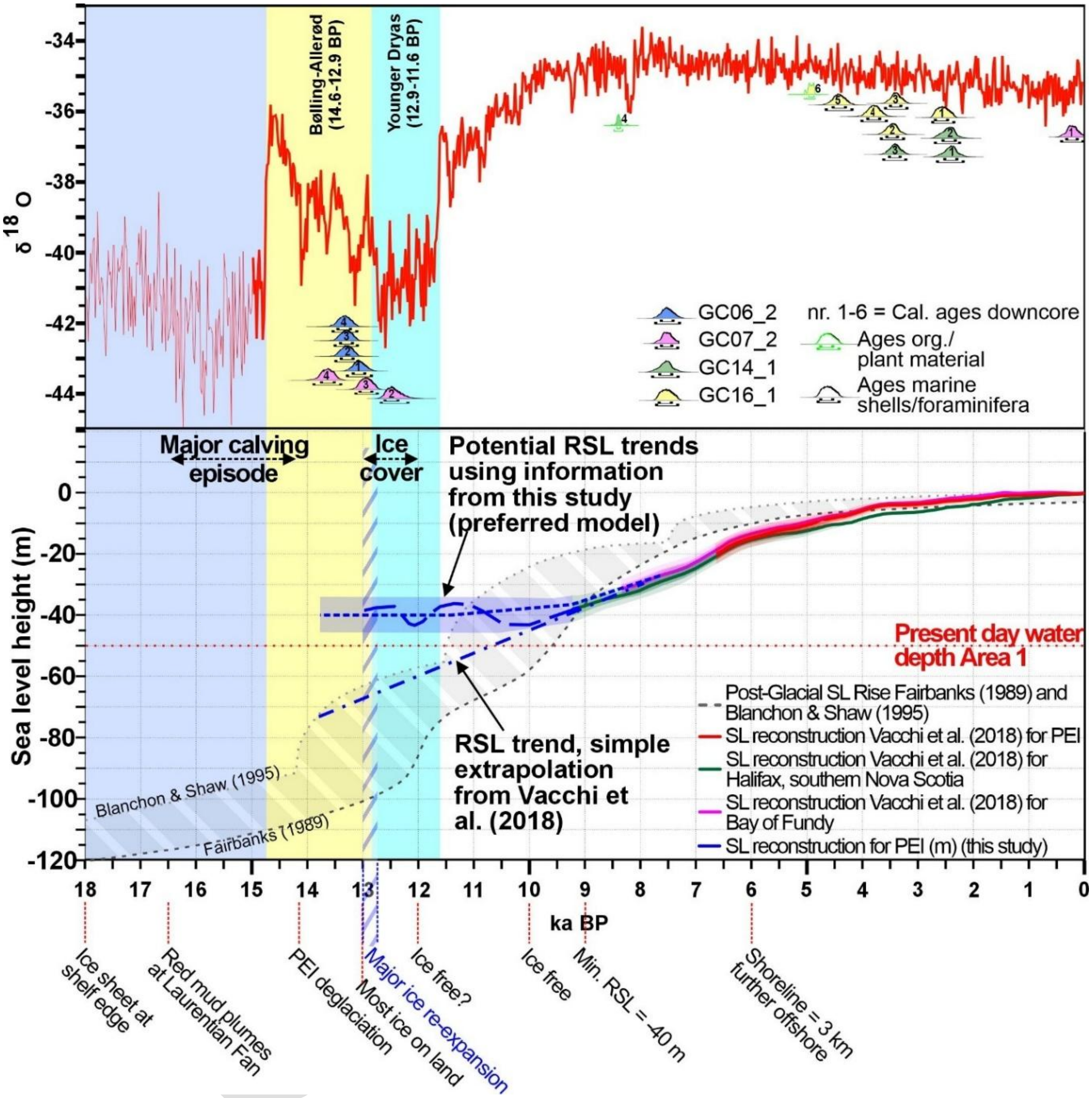

Fig. 9: Top: Age estimates from five sediment cores collected in the southern Gulf of St. Lawrence calibrated using the software OxCal (version 4.4). Data are plotted along the δ^{18}O-curve (red line; from Ramsey, 2021). Bottom: Comparison of various sea level (SL) curves on a regional (Vacchi et al., 2018) and global scale (modified from Fairbanks (1989) and Blanchon & Shaw (1995)) that show similar trends and RSL curves (three blue dotted lines) reconstructed for the research area pre-9 ka BP using findings in this study. Important events described in the literature are highlighted below the graphic (Stea & Mott, 1989; Forbes et al., 2004; 2014; Shaw, 2005; Shaw et al., 2006; 2009; Skene & Piper, 2006; Stea, 2011; Vacchi et al., 2018).

5. Discussion

5.1. Bedrock geomorphology

U0 is present throughout all study sites, and often shows dipping sub-bottom reflections, especially to the east of PEI (Site 3) (Fig. 2, Table 1). We interpret U0 as representative of bedrock (Fig. 10), which in the Maritime Basin are represented by the Carboniferous to Permian sandstones that are also described as flat dipping (Carr, 1969; Symons, 1990; Van de Poll, 1989). Horizon R1 forms the boundary between these "redbeds" and the overlying unconsolidated sediments (Fig. 2). Mapping of R1 exposes various, presently buried depressions within the bedrock (Figs. 6a, c & e, 10). The up to 35 m deep depressions to the north of PEI (Site 1) strongly resemble basins, given their isolated appearance (Figs. 3, 6a). They are oriented parallel to the modern PEI coastline and within these basins several topographic elevations are observable (Figs. 3, 6a). Given these characteristics, it is possible that the basins were formed by glacial erosion (Fig. 10) (cf. Cook & Swift, 2012; Patton et al., 2016). To the east (Site 3) and especially northeast of PEI (Site 2), R1 reveals numerous EW- to NE-trending elongated depressions within the bedrock, which resemble channels with some being directed towards the CBT (Figs. 1a & b, 6c & e). Channels observed within Site 2 occur in fact in vicinity to present-day EW-oriented seafloor channels located between PEI and the Magdalen Islands (Figs. 1b), which were previously interpreted as tunnel valleys (Loring & Nota, 1973). It is thus plausible that the presently buried channel systems observed within Sites 2 and 3 are remains of tunnel valleys (cf. Loring & Nota, 1973; Shaw et al., 2006; Pinet & Brake, 2024) or low stand, fluvial river systems (Fig. 10) (cf. Pinet & Brake, 2024).

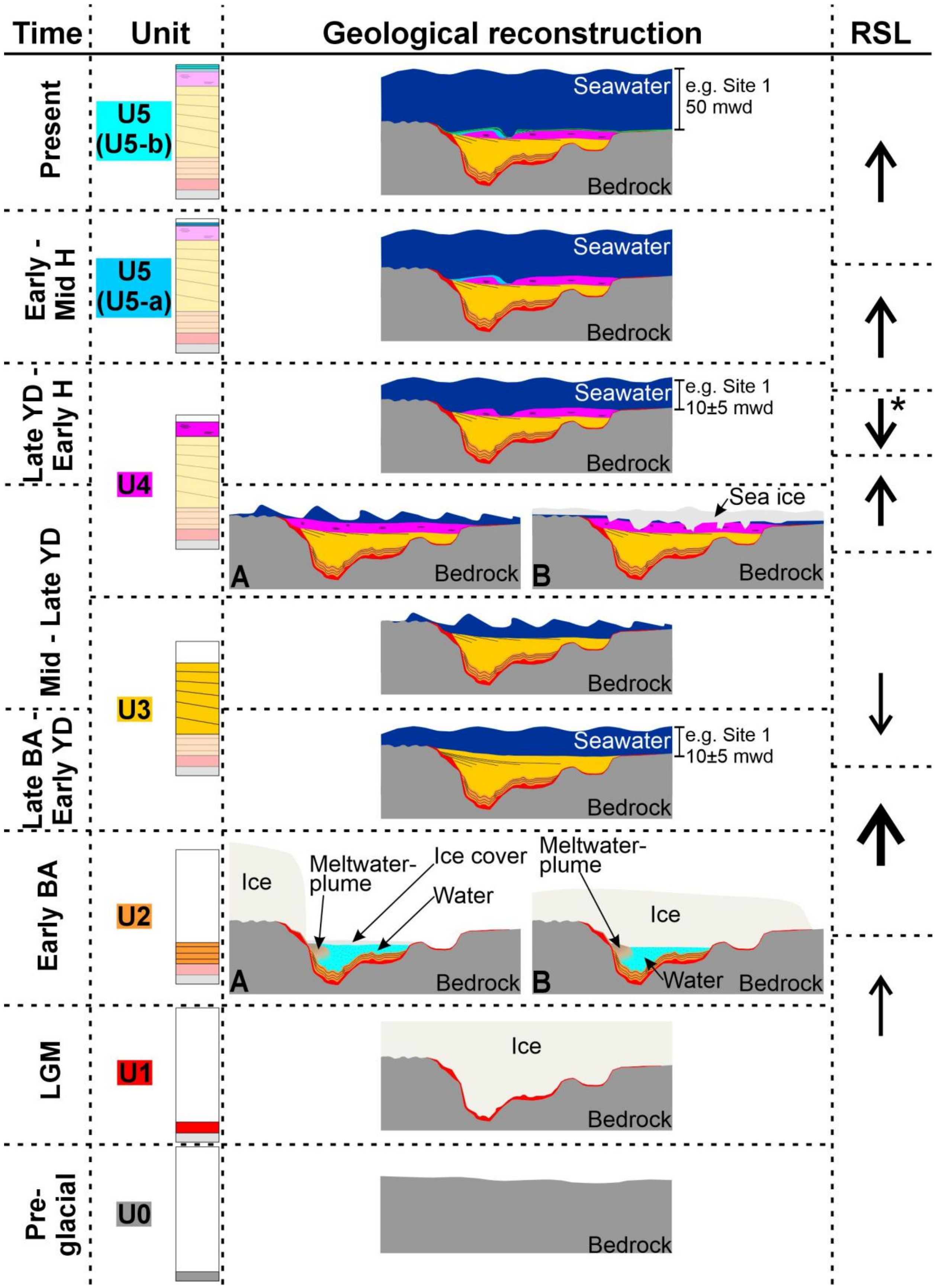
Time
Unit
Geological reconstruction
RSL
Present
U5
(U5-b)
Seawater
e.g. Site 1
50 mwd
Bedrock
Early - Mid H
U5
(U5-a)
Seawater
Bedrock
Late YD - Early H
Seawater
e.g. Site 1
10±5 mwd
Bedrock
*
U4
Mid - Late YD
Sea ice
A
Bedrock
B
Bedrock
Bedrock
U3
Late BA - Early YD
Seawater
e.g. Site 1
10±5 mwd
Bedrock
Early BA
U2
Ice
Meltwater-
plume
Ice cover
Water
A
Bedrock
Meltwater-
plume
Ice
B
Water
Bedrock
LGM
U1
Ice
Bedrock
Pre-
glacial
U0
Bedrock

515

Fig. 10: Geological reconstruction of the stratigraphic and sedimentological evolution of the study area from the LGM to present. Acronyms are as follow: LGM = Last Glacial Maximum, BA = Bølling-Allerød, YD = Younger Dryas, and H = Holocene. A and B panels represent different possible interpretations for the deposition of U2 and U4. The arrows indicate the estimated rate of sea level change with thicker arrows indicating a higher rate. The sea level drop with star is based on previous findings such as reported in Shaw (2005), Forbes et al. (2014) and Vacchi et al. (2018).

5.2. Late Pleistocene and Holocene depositional reconstruction

5.2.1. Last Glacial Maximum

U1 is the lowermost depositional unit within all basins and channels in the research area (Fig. 2). Given the acoustic response of U1 (transparent with no apparent sub-bottom reflections) and its variable thickness (2-9 m thick) distribution we interpret this unit as glacial till (cf. Josenhans et al., 1986; Josenhans & Fader, 1989; Zecchin & Rebesco, 2018) (Figs. 2, 5; 10; Table 1), which was likely deposited when the LIS occupied the Gulf of St. Lawrence (Loring & Nota, 1973). The glacial till (U1) directly overlies the bedrock (R1, U0) (Fig. 2), which indicates that the ice was grounded during deposition of U1 within the basins and channels (Josenhans & Lehmann, 1999; Shaw et al., 2006), and supports the interpretation that these basins and channels were indeed formed from subglacial erosion and by meltwater flows (Fig. 10) (cf. Loring & Nota, 1973; Cook & Swift, 2012; Patton et al., 2016). Basins and channels are still evident within horizon R2 (Figs. 3, 4), although their width is reduced due to the infill with glacial till (Figs. S3, S4, S5).

5.2.2. Bølling-Allerød and Younger Dryas

The stratified nature of U2 and U3, and association of U3 reflection characteristics to clayey mud with interbedded sand (GC06_2, GC07_2) on top of U1 suggests that these units represent glaciolacustrine, glaciomarine or marine sediments (Fig. 11) (cf. Josenhans et al., 1986; Josenhans & Fader, 1989; Zecchin et al., 2016). Radiocarbon dating confirms U3 as of late Bølling-Allerød (13.6-12.9 ka cal BP) to early Younger Dryas (12.9-12.5 ka cal BP) age (Figs. 7, 9; Table 2), and consequently places the deposition of U2, not dated directly, after the LGM and before the late Bølling-Allerød.

5.2.2.1. Early Bølling-Allerød

U2 shows conformable, low amplitude reflection characteristics (Table 1). Sediments with such a seismic response have been interpreted elsewhere as ice proximal to distal glaciolacustrine or glaciomarine mud with layers of ice rafted debris that were deposited within a low-energy environment, primarily from suspension clouds in association with sediment-laden meltwater or hyperpycnal flows (e.g., Josenhans & Fader, 1989; Josenhans et al., 1990; Garcia-Garcia et al., 2004; Zecchin & Rebesco, 2018; Hogan et al., 2020; Dhavamani et al., 2022).

The age and distribution of U2 within deeper basin and channel portions (15-35 m deep) suggest deposition in front or underneath the retreating LIS (Figs. 5a & b, 10). These deeper regions were possibly flooded with meltwater during ice retreat generating low-energy and sheltered depositional environments, such as bays or lakes (Fig. 10). This depositional setup would explain the strong conformity of U2 reflections to horizon R2 (Fig. 10). A change in the reflection amplitude of U2 within Site 2 could be result of changes in the concentration of suspended sediment or the amount of ice rafted debris (Table 1) (c.f. Josenhans et al., 1990; Batchelor et al., 2011; Zecchin et al., 2016; Zecchin & Rebesco, 2018). Site 2 is located further offshore then Sites 1 and 3 and less secluded and was likely affected earlier by ice retreat and RSL rise, which could have facilitated a stronger deposition of ice rafted debris resulting in the higher reflection amplitudes along the sides of the channels (cf. Melles & Kuhn, 1993; Hodell et al., 2010; Klotsko et al., 2019). Given the distribution and general echo characteristic of U2, however, leads us to conclude that a marine influence on its deposition was negligible (Fig. 10).

5.2.2.2. Late Bølling-Allerød to Younger Dryas

U3 has a similar reflection characteristic to U2 (Table 1). An unconformity at the base of U3 and subsequent presence of onlapping reflections (Figs. 3, 7), however, indicates a change in the depositional environment or change in the intensity of existing processes such as a marine transgression or regression from U2 to U3 (cf. Mitchum et al., 1977). Sediment cores (GC06_2, GC07_2) from U3 consist of dark reddish-brown clayey mud interbedded with layers of fine and medium sand (Fig. 8). An abundance of fine-grained material can be associated with deposition under low-energy conditions, while the presence of sandy layers indicates a more active environment (Zecchin et al., 2016; Zecchin & Rebesco, 2018). This correlates to the abundant taxa of biofacies A, which represents marginal marine, open bay (*E. excavatum*, *E. clavatum*, *B. frigida*) or shallow marine arctic and ice-proximal conditions with variable salinity and sediment supply (e.g., Schafer & Cole, 1982; Scott et al., 1977, 1980, 2001; Rodrigues & Hooper, 1982; Hald &

Korsun, 1997). U3 further shows a significant change in the sedimentation rate from ~0.1 cm a^{-1} during the late Bølling-Allerød to ~1 cm a^{-1} during the early Younger Dryas.

The low sedimentation rates during the late Bølling-Allerød in the lower portion of U3 are possibly a consequence of the interplay between the absent LIS, which previously affected the deposition of U2, and marine transgression that we interpret as primarily cause for the unconformity at horizon R3 (Figs. 4, 10). In addition, wave and tide action in shallow marine water may have facilitated erosion rather than deposition (cf. Forbes et al., 2014). The shift to high sedimentation rates within the majority of U3 indicates a change in the depositional conditions. Analyzing glaciomarine sediments from the St. Lawrence Estuary and Laurentian Channel, Loring and Nota (1973) argued sedimentation in front of re-advancing ice masses during the Younger Dryas cooling event caused high sedimentation rates. While the extent of a Younger Dryas ice mass is a matter of debate (Stea & Mott, 1998), the distribution and age of U3 suggests that deteriorating conditions with possible ice built up during the Younger Dryas caused a transition to high sedimentation rates in the research area. We associate the erosional truncation at the top of U3 (horizon R4) with a drop in RSL potentially due to ice buildup and increased storm and subsequent wave activity because of further deteriorating climate conditions (Fig. 10) (cf. Brauer et al., 2008; Slowinski et al., 2017). The seaward inclination of this unconformity (horizon R4) supports this interpretation (Fig. 6b & d).

5.2.3. Late Younger Dryas and early Holocene

The echo characteristic of U4 (chaotic with interbedded parallel reflections) strongly contrasts with those of U3 (Fig. 2, Table 1). Papatheodorou et al. (2021) observed a similar echo-characteristic to U4 in the central Ionian Sea and interpreted them as a result of soft-sediment deformation. There is, however, no definitive sediment sample from U4, as the medium to coarse sand with pieces of gravel at the tops of GC06_2 and GC07_2 could be sediment material from either U4 or U5 (Figs. 7, 8).

Radiocarbon dating of the units below and above U4 reveals that its deposition occurred after 12.5 ka cal BP and before 9 ka cal BP (Figs. 7, 9; Table 2). This time interval primarily describes the Younger Dryas, which likely saw an ice re-advance from isolated marine and terrestrial ice remnants on PEI and Nova Scotia (Dalton et al., 2024; Stea & Mott, 1989; 2005; Shaw et al., 2006, Stea, 2011, Vacchi et al., 2018). An absence of geological features such as moraines, drumlins or eskers along horizons R4 and R5, however, indicates that the ice mass was not grounded in our study sites (Fig. 9) (Shaw, 2005; Shaw et al., 2006; 2009). We observe inclined sediment layers at the base of U4 with a wedge-shaped appearance near the coast of Cape Breton (Fig. 5b, S6), which are characteristic attributes for subaqueous fans that often form in front of the grounding line of floating ice or glaciers (Dowdeswell & Fugelli, 2012). Alternatively, the inclined sediment layers could be part of a flood delta. Stea and Mott (1989; 1998) found evidence for such flooding events by analyzing deltas within glacial lakes in Nova Scotia that resulted from breached ice dammed lakes.

We, therefore, interpret U4 as ice proximal sediment either from: 1) meltwater-derived sedimentation in front of and underneath a floating ice margin; or 2) deposition from a catastrophic flooding event. We further consider two possible processes to explain the chaotic reflection characteristic of U4 deposits (Figs. 3, 7; Table 1). Firstly, sediment disturbance is introduced from sea ice or floating ice in front of the ice masses centered on PEI and Nova Scotia (Fig. 10). The floating ice froze and subsequently sheared the upper sediment strata of U4. Present-day multiyear sea ice in Antarctica is up to 10 m thick as a result of ice deformation (Goosse et al., 2013), which shows that Younger Dryas sea ice offshore PEI could have been in direct contact with the sediment proximal to the coast. Secondly, an increase in sea level, but with shallow water coverage allowing a high influence of waves and tides, was probably enhanced by the intensification of winds and storms during the Younger Dryas (Fig. 10) (cf. Brauer et al., 2008, Toomey et al., 2017). In this scenario we suggest that the waves and tide action deposited and continuously reworked U4 (cf. Forbes et al., 2014).

5.2.4. Holocene sedimentation

U5 consists of fine- to coarse-grained sandy mud and muddy sand of Holocene age (11.6 ka BP to present) (Fig. 8; Table 2). The lower portion or U5-a is up to 4 m thick and is present within elongated depressions (Site 1) and channels (Site 2 & 3), while the upper portion or U5-b is only 0.5 to 1 m thick but present throughout the research area (Figs. 3, 5b). U5 overall displays parallel, stratified reflections (Fig. 2). Exceptions are found north of PEI (Site 1) and locally northeast of

PEI (Site 2). North of PEI (Site 1), U5 migrates into and abruptly terminates within the elongated depressions present along the modern seafloor (Figs. 1c, 3). The unit shows reflection downlaps, which resemble sediment drifts from bottom currents observed in other areas such as the Barents Sea (Zecchin et al., 2016; Rebesco et al., 2016). Northeast of PEI (Site 2) but only within U5-a, localised reflection downlaps are observable that are associated with buried channel structures (Fig. 4). These channels occur in higher water depth (90 mwd) than sediment drifts observed to the north of PEI (50 mwd) (Fig. 1b). The acoustic response within U5-a resembles multicycle incisions found within former meandering channel systems or erosional channel belts (cf. Janocko et al., 2013; Dubey et al., 2019). They are often associated with sea level fluctuations and consequent changes in the hydraulic energy condition (Janocko et al., 2013; Dubey et al., 2019).

Sediment cores from U5 contain Biofacies A (lower part of GC16_2), B (GC14_2) and C (upper part of GC16_2) and indicate a similar depositional trend (Table S2). The taxa indicate a shift from shallow marine conditions (*E. excavatum*, *E. clavatum*, *B. frigida*, Rodrigues & Hooper, 1982; Schafer & Cole, 1982; Scott et al., 1977, 1980, 2001) during the early Holocene to conditions with strong salinity and temperature gradients during the late Holocene (*L. atlantica* previously known as *Saccamina atlantica,* Williamson et al., 1984). The late Holocene taxa further indicate a high flux of organic matter with a dominance of taxa associated with cold and well oxygenated bottom water (*L. difflugiformis* in biofacies C*,* Vilks et al., 1982; Jennings & Helgadottir, 1994; Alve et al., 2016) <20 km from PEI (GC16_2) and low oxygen conditions further offshore (>20 km) (GC14_2, *N. labradorica* & *I. helenae* of biofacies B, Hald & Korsun, 1997; Bernhard & Bowser, 1999; Rytter et al., 2002; Cage et al., 2021; Schmidt et al., 2022; Racine et al., 2023).

In conclusion, the topmost sediment unit, U5, shows both Holocene drift deposits strongly influenced by bottom, or in this case more likely coastal, currents in the shallower parts of the shelf and localised occurrence of multicycle, buried channel systems in the deeper, eastern sections of the research area (Figs. 3, 4). A change in the environment conditions is further evident through the occurrence of an erosional truncation (horizon R6) within U5 (Fig. 3; Table 1), which likely results from sea level fluctuation during the Holocene. U5-a was likely deposited during the early Holocene when the sea level rose rapidly, while U5-b was deposited more recently during lower rates of sea level rise (Fig. 10) (cf. Forbes et al., 2004, 2014).

5.3. Specific depositional or post-depositional formations

Transparent, wedge- and pocket shaped features that we observed within U3 (Figs. 3, 5, 7) are potentially associated with rapid sedimentation of this unit given that similar features are described in association with cut and fill and sediment loading elsewhere (e.g., Kleiber et al., 2001; Fulthorpe & Austin, 2004; Correggiari et al. 2005). Acoustic blanking can, nevertheless, also be an indication for the presence of a significant (>2% of pore space) amount of free gas in sediments (Lohrberg et al., 2020). Such gas accumulations, which may be produced by in situ degradation of organic matter in the presence of low permeability, however, absorb the seismic signal generating acoustic blanking of layers underneath, but it is not the case here (Figs. 3, 7). Transparent, funnel-shaped features that resemble our wedge-shaped features have been reported offshore New Zealand and interpreted as buried pockmarks that were formed by vertical fluid flow (Micallef et al., 2022). Interestingly, we observe dome-shaped features with low amplitude to no sub-bottom reflections in sub-bottom profiles north of PEI (Site 1), in vicinity to the wedge-shaped features of U3 (Fig. 3). These dome-shaped features also resemble fluid plumes observed in sub-bottom profiles and seismic reflection profiles elsewhere (e.g., Trincardi et al., 2004; Lundmark, 2017; Papatheodorou et al., 2021), which may indicate that both, wedge-shaped and dome-shaped features, may have resulted from similar mechanisms.

The fluid plumes described in the literature, however, often extend through the sediment package to the seafloor. Furthermore, the funnel-shaped features observed offshore New Zealand show a much larger size with >50 m vertical extension than the ones observed in our study (<5 m high) and lateral amplitude reductions are observable underneath these features (Micallef et al., 2022). They, thus, stronger resemble acoustic blank features observed within Holocene sediments (U5) deposited northeast of PEI (Site 2). We, therefore, interpret wedge-shaped features observed within U5 in Site 2 as result of fluid expulsion, potentially consisting of gas, while those in U3 are either a direct result of rapid sediment deposition or also fluid expulsion, but its unclear if this is gas related. Coincidently, the dome-shaped features are likely related to fluid expulsion, but at this stage further data and analysis are needed to indicate the nature of these dome-shaped features.

5.4. Indications of ice advance and retreat and the influence on sea level

Based on the distribution of reflection characteristics and results from our sediment core analysis, we propose a model for the changes in RSL that affected the research area during the last 18 ka BP (sections 5.1 and 5.2) (Fig. 11). Except for minor modifications, the new findings agree well with previous reconstructions such as shown in Dyke et al. (2003), Shaw et al. (2006) and Dalton et al. (2020; 2024).

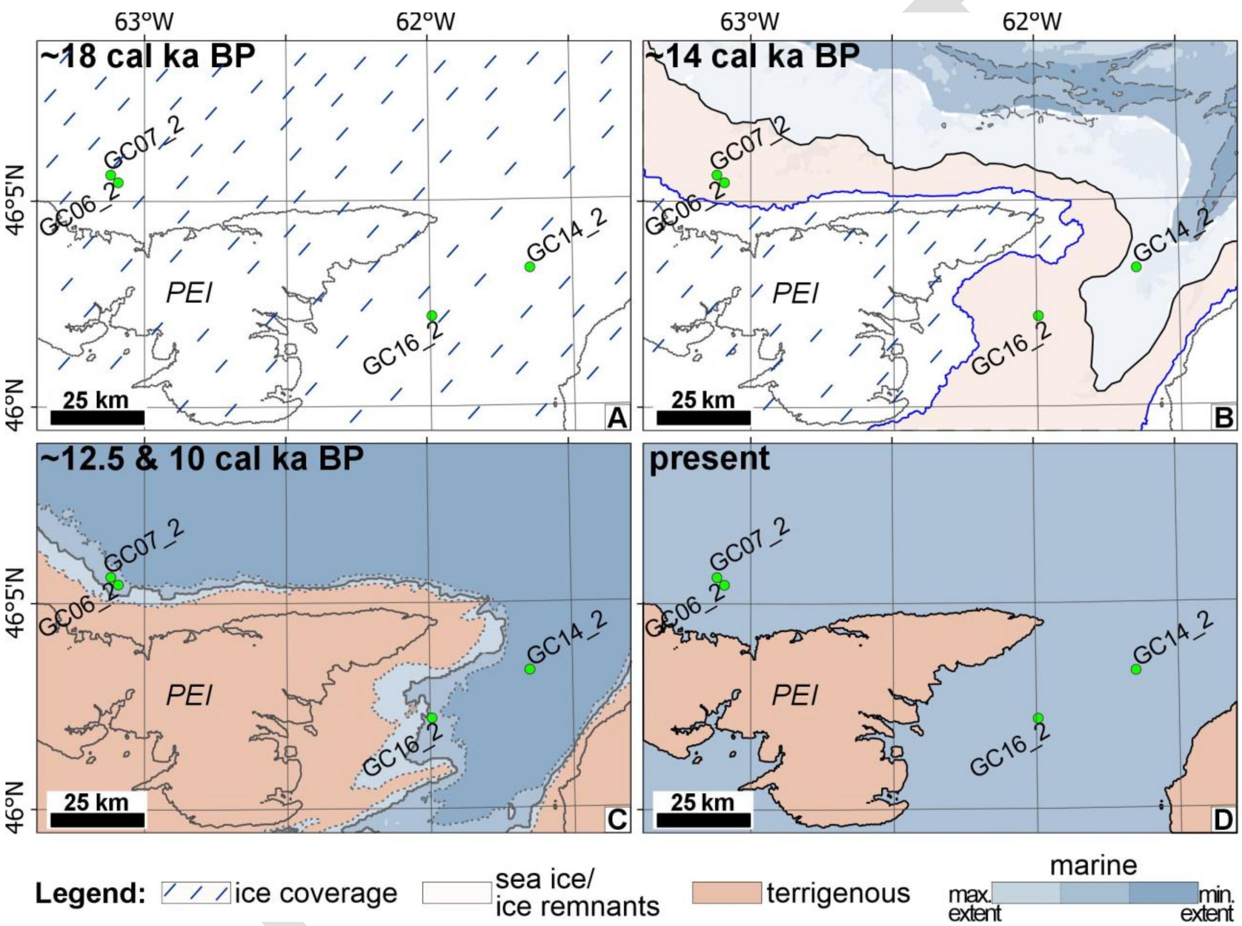

Fig. 11: Potential development of the absolute Sea Level within the research area under consideration of findings in this study. The panels show A) coverage of the research area underneath the Laurentide Ice Shield (LIS) around 18 ka BP, B) retreat of the ice mass onshore with blue line indicating its approximate estimated extent, and extent of sea ice or presence of ice remnants (transparent white surface) as well as apparent local sea level at 14 ka BP, C) local sea level stand around 12.5 and 10 ka BP, and D) modern sea level. Note that the sea level in B and C is shown with a minimum and maximum extent as highlighted by the different color and dotted lines.

5.4.1. 18 ka cal BP

The LIS covered the entire continental shelf of Atlantic Canada down to the continental slope, while the global sea level was ~120 m below the modern sea level (e.g., Fairbanks, 1989; Shaw et al., 2006; Forbes et al., 2014; McHugh et al., 2010) (Fig. 9). The entire research area, therefore, was covered by ice during the LGM (Fig. 11a) resulting in the deposition of glacial till (U1) (Fig. 2; Table 1).

5.4.2. 14 ka cal BP

Deglaciation with rapid ice disintegration and massive calving events started ~16 ka BP in the Gulf of St. Lawrence (Shaw, 2005). The ice margin likely reached PEI and the Magdalen Islands after ~14.1 ka BP and likely ended up onshore between 13.5 and 13 ka BP (Vacchi et al., 2018). Extrapolating sea level curves from Vacchi et al. (2018) in regard to global sea level trends (Fairbanks, 1989; Blanchon & Shaw, 1995) yields a sea level height ~70 m below the modern sea level at 14 ka BP (Fig. 9).

The unconformity at the base of U3 (horizon R3) and subsequent deposition of marine sediments (U3) as old as 13.6 ka BP, however, suggests an earlier retreat of the ice and a marine transgression as early as 13.6 ka BP (Figs. 9, 11b). We, therefore, propose that at ~14 ka BP the sea level was already 70 to 50 m below the modern sea level and that the ice mass was either in proximity to the modern coastline (e.g., -30 m isobath) or centered on PEI (Fig. 11b). This interpretation differs from the reconstruction of Dyke et al. (2003), Shaw et al. (2006) and Dalton et al. (2020; 2024) who illustrated full ice coverage into the Gulf of St. Lawrence across our study site north of PEI (Site 1) at 14 ka BP. We interpret that U2 deposition during the Early Bølling-Allerød (14.6-13.6 ka BP) was primarily in front or underneath the retreating LIS. Deposition of U2, past 14 ka BP, was likely facilitated underneath ice remnants or sea ice that still covered the study sites, as the front of the ice retreated behind the sites. PEI was ice free between 12 and 10 ka BP (Fig. 9) (Vacchi et al., 2018).

5.4.3. 12.5 to 10 ka cal BP

The pre- and proglacial basins and channels were filled with U2 and U3 sediments by 12.5 ka cal BP (Figs. 3, 7). Foraminifera from U3 sediments from our study site north of PEI (Site 1) indicate a deposition under shallow marine conditions between 13.6 and 12.5 ka cal BP (Figs. 9, 11c).

Currently the seafloor in Site 1 is at 40 to 50 mwd (Fig. 1b). If we assume a minimum water depth of 10±5 m during the deposition of U3, then this would suggest that local sea level was 40±5 m below the modern one at 12.5 ka cal BP (Fig. 9). A short-term sea level rise between 12 and 10 ka cal BP is possible, as argued by others (e.g., Person et al., 2003; Forbes et al., 2014; Vacchi et al., 2018), which in our model fits within the ±5 m uncertainty (Figs. 9, 11c). Extrapolating the sea level curves from Vacchi et al. (2018) shows that at 10 ka cal BP the sea level was still 40±5 m below the modern sea level (Figs. 9, 11c). This finding agrees well with results from previous studies that estimated a sea level height of 40 m below the modern sea level from 10 to 9 ka cal BP, when wide sections of the modern shelf were exposed to subaerial conditions (Forbes et al., 2004; 2014; Shaw, 2005; Vacchi et al., 2018).

5.4.4. 10 ka cal BP to present day

Isostatic subsidence in response to ice removal, subsequent migration of the forebulge and hydro-isostatic loading led to a RSL rise, especially during the early Holocene (Person et al., 2003; Forbes et al., 2004; 2014). It is likely that the erosional truncation at horizon R6 and consequent change in the development of sinuous channels or the extent of sediment drifts within U5 are a direct consequence of the change in RSL and thus hydraulic regime during the early phase of the Holocene (Fig. 3, Table 1). The current sea level extent resulted from a continuous RSL rise during the Holocene with present day rates of 3.2 mm a^{-1} (Fig. 11d) (Forbes et al., 2004; Shaw, 2005; Vacchi et al., 2018).

6. Conclusion

The landscape of the Gulf of St. Lawrence offshore PEI, as a formerly glaciated continental shelf, was strongly affected by the Pleistocene glaciations. Using sub-bottom profiles and data extracted from sediment cores, we were able to reconstruct the sedimentation history since the LGM. Our study shows that the last glaciation, as well as the Younger Dryas cooling event, significantly altered the morphology and influenced sedimentation in the region. Numerous buried sediment basins and channels are present down to 40 m sub-bottom depth, which were likely formed as a result of glacial erosion. They are entirely filled with late Pleistocene glaciolacustrine to marine sediments (13.6-12.5 ka cal BP), deposited primarily under shallow marine conditions with sedimentation rates as high as 1 cm a^{-1} during the early Younger Dryas. We argue that this rapid sedimentation occurred in connection with large amounts of sediment material being redistributed offshore in front of readvancing new ice masses, as the climate deteriorated. We further observe an erosional truncation of the sediment package deposited during the early- to mid-Younger Dryas, which we associate with a potential drop in RSL that is possibly related to ice built up. It appears, however, that the RSL subsequently rose given the presence of an up to 4 m thick sediment package on top of the erosional truncation that likely deposited between the mid-Younger Dryas and early Holocene. Given its timing and thickness distribution, we suggest that this sediment package either resulted from meltwater deposition or deposition from flooding events e.g., breaching of ice-dammed lakes. Its chaotic appearance with interbedded parallel reflections indicates sediment disturbance possibly as a result of storm waves or sea ice grounding. These layers are overlain by Holocene sediments that are locally up to 7 m thick, indicating a change from more turbulent to calm sedimentation condition.

This study provides one of the few examples of actual dated Younger Dryas sediments in Atlantic Canada. The findings show strong evidence that the Younger Dryas cooling event had in fact a large influence on sedimentation within the research area, as the largest portion of sediments were deposited during the relatively short duration of this event (1,300 a). It further presents that the Younger Dryas had some influence on the RSL development in the region that was depicted in previous models, but here we show that there may have been an additional sea level drop before the Holocene.

7. Acknowledgements

This study has been supported by the SOURCE Project funded by the Ocean Frontier Institute. We are grateful to the crew of the research expedition MSM103.The software ps32sgy developed by Hanno Keil (University of Bremen) was used to convert Parasound data into SEG-Y formats usable in Kingdom Suite™.

8. References

Alve, E., Korsun, S., Schönfeld, J., Dijkstra, N., Golikova, E., Hess, S., Husum, K., and Panieri, G. 2016. Foram-AMBI: A sensitivity index based on benthic foraminiferal faunas from North-

East Atlantic and Arctic fjords, continental shelves and slopes. Marine Micropaleontology, 122: 1-12.

Barlow, P.M. and Reichard, E.G., 2010. Saltwater intrusion in coastal regions of North America. Hydrogeology Journal, 18(1), p.247.

Batchelor, C.L., Dowdeswell, J.A. and Hogan, K.A., 2011. Late Quaternary ice flow and sediment delivery through Hinlopen Trough, Northern Svalbard margin: Submarine landforms and depositional fan. Marine Geology, 284(1-4), pp.13-27.

Bernhard, J.M. and Bowser, S.S. 1999. Benthic foraminifera of dysoxic sediments: chloroplast sequestration and functional morphology. Earth-Science Reviews, 46: 149-165.

Blanchon, P. and Shaw, J., 1995. Reef drowning during the last deglaciation: evidence for catastrophic sea-level rise and ice-sheet collapse. Geology, 23(1), pp.4-8.

Brady, H.B.1884. Report on the foraminifera dredged by HMS Challenger, during the years 1873-1876: Report on the Scientific Results of the Voyage of HMS Challenger, Zoology, 9: 1-814.

Brauer, A., Haug, G.H., Dulski, P., Sigman, D.M. and Negendank, J.F., 2008. An abrupt wind shift in western Europe at the onset of the Younger Dryas cold period. Nature Geoscience, 1(8), pp.520-523.

Cage, A.G., Pieńkowski, A.J., Jennings, A., Knudsen, K.L. and Seidenkrantz, M.S. 2021. Comparative analysis of six common foraminiferal species of the genera Cassidulina, Paracassidulina, and Islandiella from the Arctic-North Atlantic domain. Journal of Micropalaeontology, 40: 37-60.

Carr, P.A., 1969. Salt-water intrusion in Prince Edward Island. Canadian Journal of Earth Sciences, 6(1), pp.63-74.

Clark, P.U., Dyke, A.S., Shakun, J.D., Carlson, A.E., Clark, J., Wohlfarth, B., Mitrovica, J.X., Hostetler, S.W. and McCabe, A.M., 2009. The last glacial maximum. science, 325(5941), pp.710-714.

Cook, S.J. and Swift, D.A., 2012. Subglacial basins: Their origin and importance in glacial systems and landscapes. Earth-Science Reviews, 115(4), pp.332-372.

Correggiari, A., Cattaneo, A. and Trincardi, F., 2005. The modern Po Delta system: lobe switching and asymmetric prodelta growth. Marine Geology, 222, pp.49-74.

Dalton, A.S., Margold, M., Stokes, C.R., Tarasov, L., Dyke, A.S., Adams, R.S., Allard, S., Arends, H.E., Atkinson, N., Attig, J.W. and Barnett, P.J., 2020. An updated radiocarbon-based ice margin chronology for the last deglaciation of the North American Ice Sheet Complex. Quaternary Science Reviews, 234, p.106223.

Dalton, A.S., Margold, M., Dulfer, H.E., Norris, S.L. and Tarasov, L., 2024. Response of North American ice sheets to the Younger Dryas cold reversal (12.9 to 11.7 ka). Earth-Science Reviews, 255, p.104845.

Dhavamani, R., Pipík, R., Sočuvka, V., Šurka, J., Starek, D., Milovský, R., Uhlík, P., Vidhya, M., Žatková, L. and Kráľ, P., 2022. Sub-bottom and bathymetry sonar inspection of postglacial lacustrine infill of the alpine lakes (Tatra Mts., Slovakia). Catena, 209, p.105787.

Dowdeswell, J.A. and Fugelli, E.M.G., 2012. The seismic architecture and geometry of grounding-zone wedges formed at the marine margins of past ice sheets. Bulletin, 124(11-12), pp.1750-1761.

Dubey, K.M., Chaubey, A.K., Mahale, V.P. and Karisiddaiah, S.M., 2019. Buried channels provide keys to infer Quaternary stratigraphic and paleo-environmental changes: a case study from the west coast of India. Geoscience Frontiers, 10(4), pp.1577-1595.

Dyke, A.S., Moore, A. And Robertson, L., 2003: Deglaciation of North America, Geological Survey of Canada Open File 1574. https://doi.org/10.4095/214399.

Edmunds, W.M., Hinsby, K., Marlin, C., Condesso de Melo, M.T., Manzano, M., Vaikmae, R. and Travi, Y., 2001. Evolution of groundwater systems at the European coastline. Geological Society, London, Special Publications, 189(1), pp.289-311.

Evans, D.J. and Evans, I.S., 2022. Glacial processes and landforms. Geol. Soc. Lond. Mem., 58 (2022), pp. 333-377, 10.1144/M58-2021-17.

Fairbanks, R.G., 1989. A 17,000-year glacio-eustatic sea level record: influence of glacial melting rates on the Younger Dryas event and deep-ocean circulation. Nature, 342(6250), pp.637-642.

Forbes, D.L., Parkes, G.S., Manson, G.K. and Ketch, L.A., 2004. Storms and shoreline retreat in the southern Gulf of St. Lawrence. Marine Geology, 210(1-4), pp.169-204.

Forbes, D.L., Manson, G.K., Whalen, D.J.R., Couture, N.J. and Hill, P.R., 2014. Coastal products of marine transgression in cold-temperate and high-latitude coastal-plain settings: Gulf of St Lawrence and Beaufort Sea. Geological Society, London, Special Publications, 388(1), pp.131-163.

Fulthorpe, C.S. and Austin Jr, J.A., 2004. Shallowly buried, enigmatic seismic stratigraphy on the New Jersey outer shelf: Evidence for latest Pleistocene catastrophic erosion? Geology, 32(12), pp.1013-1016.

García-García, A., García-Gil, S. and Vilas, F., 2004. Echo characters and recent sedimentary processes as indicated by high-resolution sub-bottom profiling in Ría de Vigo (NW Spain). Geo-Marine Letters, 24, pp.32-45.

Gibling, M.R., Culshaw, N., Pascucci, V., Waldron, J.W.F. and Rygel, M.C., 2019. The Maritimes Basin of Atlantic Canada: Basin creation and destruction during the Paleozoic assembly of Pangea. In The sedimentary basins of the United States and Canada (pp. 267-314). Elsevier.

Goosse, H., Roche, D.M., Mairesse, A. and Berger, M., 2013. Modelling past sea ice changes. Quaternary Science Reviews, 79, pp.191-206.

Hald, M., and Korsun, S. 1997. Distribution of modern benthic foraminifera from fjords of Svalbard, European Arctic. Journal of Foraminiferal Research, 27: 101-122.

Hansen, H.J. and Lykke-Andersen, A.L. 1976. Wall structure and classification of fossil and recent elphidiid and nonionid Foraminifera. Fossils and Strata, 10: 1-37.

Hayward, B.W., Le Coze, F., Vachard, D., Gross, O. 2025. World Foraminifera Database. Accessed at https://www.marinespecies.org/foraminifera on 2025-02-09. doi:10.14284/305.

Heaton, T.J., Köhler, P., Butzin, M., Bard, E., Reimer, R.W., Austin, W.E., Ramsey, C.B., Grootes, P.M., Hughen, K.A., Kromer, B. and Reimer, P.J., 2020. Marine20—the marine radiocarbon age calibration curve (0–55,000 cal BP). Radiocarbon, 62(4), pp.779-820.

Hodell, D.A., Evans, H.F., Channell, J.E. and Curtis, J.H., 2010. Phase relationships of North Atlantic ice-rafted debris and surface-deep climate proxies during the last glacial period. Quaternary Science Reviews, 29(27-28), pp.3875-3886.

Hogan, K.A., Jakobsson, M., Mayer, L., Reilly, B.T., Jennings, A.E., Stoner, J.S., Nielsen, T., Andresen, K.J., Nørmark, E., Heirman, K.A. and Kamla, E., 2020. Glacial sedimentation, fluxes and erosion rates associated with ice retreat in Petermann Fjord and Nares Strait, north-west Greenland. The Cryosphere, 14(1), pp.261-286.

Hölz, S., 2022. Groundwater Resources Offshore Prince Edward Island, Canada Cruise No. MSM103, 12.9.–15.11. 2021 Emden (Germany)–Halifax (Canada)–Emden (Germany); PRINCE.

IPCC, 2023: Climate Change 2023: Synthesis Report. Contribution of Working Groups I, II and III to the Sixth Assessment Report of the Intergovernmental Panel on Climate Change [Core Writing Team, H. Lee and J. Romero (eds.)]. IPCC, Geneva, Switzerland, pp. 35-115, doi: 10.59327/IPCC/AR6-9789291691647.

Janocko, M.N.W.H.S.W.M., Nemec, W., Henriksen, S. and Warchoł, M., 2013. The diversity of deep-water sinuous channel belts and slope valley-fill complexes. Marine and Petroleum Geology, 41, pp.7-34.

Jennings, A.E. and Helgadottir, G. 1994. Foraminiferal assemblages from the fjords and shelf of eastern Greenland. Journal of Foraminiferal Research, 24: 123-144.

Jiang, Y. and Somers, G., 2009. Modeling effects of nitrate from non-point sources on groundwater quality in an agricultural watershed in Prince Edward Island, Canada. Hydrogeology Journal, 17(3), p.707.

Josenhans, H.W. and Fader, G.B.J., 1989. A comparison of models of glacial sedimentation along the eastern Canadian margin. Marine Geology, 85(2-4), pp.273-300.

Josenhans, H. and Lehman, S., 1999. Late glacial stratigraphy and history of the Gulf of St. Lawrence, Canada. Canadian Journal of Earth Sciences, 36(8), pp.1327-1345.

Josenhans, H.W., Zevenhuizen, J. and Klassen, R.A., 1986. The Quaternary geology of the Labrador shelf. Canadian Journal of Earth Sciences, 23(8), pp.1190-1213.

Josenhans, H., Zevenhuizen, J. and MacLean, B., 1990. Preliminary seismostratigraphic interpretations from the Gulf of St. Lawrence. Current Research, Part B, Geological Survey of Canada, Paper, pp.59-75.

Kleiber, H.P., Niessen, F. and Weiel, D., 2001. The Late Quaternary evolution of the western Laptev Sea continental margin, Arctic Siberia—implications from sub-bottom profiling. Global and Planetary Change, 31(1-4), pp.105-124.

Klotsko, S., Driscoll, N. and Keigwin, L., 2019. Multiple meltwater discharge and ice rafting events recorded in the deglacial sediments along the Beaufort Margin, Arctic Ocean. Quaternary Science Reviews, 203, pp.185-208.

Kongsberg, 2022. EM712 – Multibeam Echo sounder, datasheet. https://www.kongsberg.com/discovery/seafloor-mapping/em/em712/. Open Document, Norway.

Lohrberg, A., Schmale, O., Ostrovsky, I., Niemann, H., Held, P. and Schneider von Deimling, J., 2020. Discovery and quantification of a widespread methane ebullition event in a coastal inlet (Baltic Sea) using a novel sonar strategy. *Scientific reports*, *10*(1), p.4393.

Loring, D.H. and Nota, D.J.G., 1973. Morphology and sediments of the Gulf of St. Lawrence. Fisheries Research Board of Canada, Bulletin, 182, 1-147.

Lundmark, K., 2017. Acoustic survey of sea floor features in Asköfjärden. BSc. thesis, Stockholm University, Stockholm, Sweden, p. 51. urn:nbn:se:su:diva-143790.

McHugh, C.M., Hartin, C.A., Mountain, G.S. and Gould, H.M., 2010. The role of glacio-eustasy in sequence formation: Mid-Atlantic Continental Margin, USA. Marine Geology, 277(1-4), pp.31-47.

McNeely R., Dyke A. S., and Southon J. R, 2006. Canadian marine reservoir ages, preliminary data assessment, Open File 5049, pp. 3. Geological Survey Canada.

Melles, M. and Kuhn, G., 1993. Sub-bottom profiling and sedimentological studies in the southern Weddell Sea, Antarctica: evidence for large-scale erosional/depositional processes. Deep Sea Research Part I: Oceanographic Research Papers, 40(4), pp.739-760.

Micallef, A., Averes, T., Hoffmann, J., Crutchley, G., Mountjoy, J.J., Person, M., Cohen, D., Woelz, S., Bury, S.J., Ahaneku, C.V. and Spatola, D., 2022. Multiple drivers and controls of pockmark formation across the Canterbury Margin, New Zealand. *Basin Research*, *34*(4), pp.1374-1399.

Mitchum Jr, R.M., Vail, P.R. and Thompson III, S., 1977. Seismic stratigraphy and global changes of sea level: Part 2. The depositional sequence as a basic unit for stratigraphic analysis: Section 2. Application of seismic reflection configuration to stratigraphic interpretation.

Papatheodorou, G., Geraga, M., Christodoulou, D., Fakiris, E., Iatrou, M., Georgiou, N., Dimas, X. and Ferentinos, G., 2021. The Battle of Lepanto search and survey mission (1971–1972) by Throckmorton, Edgerton and Yalouris: Following their traces half a century later using marine geophysics. Remote Sensing, 13(16), p.3292.

Patton, H., Swift, D.A., Clark, C.D., Livingstone, S.J. and Cook, S.J., 2016. Distribution and characteristics of overdeepenings beneath the Greenland and Antarctic ice sheets: Implications for overdeepening origin and evolution. Quaternary Science Reviews, 148, pp.128-145.

Person, M., Dugan, B., Swenson, J.B., Urbano, L., Stott, C., Taylor, J. and Willett, M., 2003. Pleistocene hydrogeology of the Atlantic continental shelf, New England. Geological Society of America Bulletin, 115(11), pp.1324-1343.

Pinet, N. and Brake, V., 2024. Aeromagnetic data reveals buried Quaternary drainage patterns in the Gulf of St Lawrence (Canada). Journal of the Geological Society, 181(6), pp.jgs2024-057.

Racine, C., Bonnin, J., Dessandier, P.-A., and Giraudeau, J. 2023. Distribution of Living Benthic Foraminifera in the Baffin Bay and Nares Strait in the Summer and Fall Periods: Relation with Environmental Parameters. Journal of Marine Sciences and Engineering, 11, 2049. https://doi.org/10.3390/jmse11112049.

Ramsey, C.B., 2009. Bayesian analysis of radiocarbon dates. Radiocarbon, 51(1), 337–360.

Ramsey, C.B., 2021. OxCal. v4.4. Available at: https://c14.arch.ox.ac.uk/oxcal.html (accessed 12 January 2024).

Rebesco, M., Özmaral, A., Urgeles, R., Accettella, D., Lucchi, R.G., Rüther, D., Winsborrow, M., Llopart, J., Caburlotto, A., Lantzsch, H. and Hanebuth, T.J., 2016. Evolution of a high-latitude sediment drift inside a glacially-carved trough based on high-resolution seismic stratigraphy (Kveithola, NW Barents Sea). Quaternary Science Reviews, 147, pp.178-193.

Reimer, P.J., Austin, W.E., Bard, E., Bayliss, A., Blackwell, P.G., Ramsey, C.B., Butzin, M., Cheng, H., Edwards, R.L., Friedrich, M. and Grootes, P.M., 2020. The IntCal20 Northern Hemisphere radiocarbon age calibration curve (0–55 cal kBP). Radiocarbon, 62(4), pp.725-757.

Rodrigues, C.G. and Hooper, K. 1982. Recent benthonic foraminiferal associations from offshore environments in the Gulf of St. Lawrence. Journal of Foraminiferal Research, 12, 4: 321-352.

Rytter, F., Knudsen, K. L., Seidenkrantz, M. S., and Eiríksson, J. 2002. Modern distribution of benthic foraminifera on the North Icelandic shelf and slope. Journal of Foraminiferal Research, 32: 217-244.

Schafer, C.T., and Cole, F.E. 1982. Living benthic foraminifera distributions on the continental slope and rise east of Newfoundland, Canada. Geological Survey of America, Bulletin, 93: 207-217.

Schmidt, C., Geslin, E., Bernhard, J.M., LeKieffre, C., Svenning, M.M., Roberge, H., Schweizer, M. and Panieri, G. 2022. Deposit-feeding of Nonionellina labradorica (foraminifera) from an Arctic methane seep site and possible association with a methanotroph. Biogeosciences, 19: 3897-3909.

Schröder-Adams, C.J., Cole, F.E., Medioli, F.S., Mudie, P. J., Scott, D.B. and Dobbin, L.1990. Recent Arctic shelf foraminifera: Seasonally ice covered vs. perennial ice-covered areas. Journal of Foraminiferal Research, 20: 8-36.

Scott, D.B., and Vilks, G. 1991. Benthonic foraminifera in the surface sediments of the deep-sea Arctic Ocean, Journal of Foraminiferal Research, 21: 20-38.

Scott, D.B., Medioli, F.S., and Schafer C.T. 1977. Temporal changes in foraminifera distributions in Miramichi River estuary New Brunswick. Canadian Journal of Earth Sciences, 14, 7: 1566-1587.

Scott, D.B., Schafer, C.T,, and Medioli, F.S.1980. Eastern Canadian estuarine Foraminifera: A framework for comparison: Journal of Foramiferal Research, 10, 3: 205-234.

Scott, D.B., Medioli, F.S., and Schafer, C.T. 2001. Monitoring in Coastal Environments using Foraminifera and Thecamoebian Indicators. Cambridge University Press, Cambridge. 177 pp.

Shaw, J., 2005. Geomorphic evidence of postglacial terrestrial environments on Atlantic Canadian continental shelves. Géographie physique et Quaternaire, 59(2), pp.141-154.

Shaw, J., Piper, D.J.W., Fader, G.B.J., King, E.L., Todd, B.J., Bell, T., Batterson, M.J. and Liverman, D.G.E., 2006. A conceptual model of the deglaciation of Atlantic Canada. Quaternary Science Reviews, 25(17-18), pp.2059-2081.

Shaw, J., Todd, B.J., Brushett, D., Parrott, D.R. and Bell, T., 2009. Late Wisconsinan glacial landsystems on Atlantic Canadian shelves: New evidence from multibeam and single-beam sonar data. Boreas, 38(1), pp.146-159.

Skene, K.I. and Piper, D.J., 2006. Late Cenozoic evolution of Laurentian Fan: development of a glacially-fed submarine fan. Marine Geology, 227(1-2), pp.67-92.

Słowiński, M., Zawiska, I., Ott, F., Noryśkiewicz, A.M., Plessen, B., Apolinarska, K., Rzodkiewicz, M., Michczyńska, D.J., Wulf, S., Skubała, P. and Kordowski, J., 2017. Differential proxy responses to late Allerød and early Younger Dryas climatic change recorded in varved sediments of the Trzechowskie palaeolake in Northern Poland. Quaternary Science Reviews, 158, pp.94-106.

Spieß, V., 1993. Digitale Sedimentechographie – Neue Wege zu einer hochauflösenden Akustostratigraphie. Berichte Fachbereich Geowissenschaften Univ. Bremen 35, 1–199.

Stanic, S., LeRoux, N.K., Paldor, A., Mohammed, A.A., Michael, H.A. and Kurylyk, B.L., 2024. Saltwater intrusion into a confined island aquifer driven by erosion, changing recharge, sea-level rise, and coastal flooding. Water Resources Research, 60(1), p.e2023WR036394.

Stea, R.R., 2011. Appalachian Glacier Complex in Maritime Canada. In: Singh, V.P., Singh, P., Haritashya, U.K. (eds) Encyclopedia of Snow, Ice and Glaciers. Encyclopedia of Earth Sciences Series. Springer, Dordrecht. https://doi.org/10.1007/978-90-481-2642-2_25

Stea, R.R. and Mott, R.J., 1989. Deglaciation environments and evidence for glaciers of Younger Dryas age in Nova Scotia, Canada. Boreas, 18(2), pp.169-187.

Stea, R.R. and Mott, R.J., 1998. Deglaciation of Nova Scotia: stratigraphy and chronology of lake sediment cores and buried organic sections. Géographie physique et Quaternaire, 52(1), pp.3-21.

Stea, R.R. and Mott, R.J., 2005. Younger Dryas glacial advance in the southern Gulf of St. Lawrence, Canada: analogue for ice inception? Boreas, 34(3), pp.345-362.

Stokes, C.R., 2017. Deglaciation of the Laurentide ice sheet from the last glacial maximum. Cuadernos de investigación geográfica, 43(2).

Symons, D.T.A., 1990. Early Permian pole: Evidence from the Pictou red beds, Prince Edward Island, Canada. Geology, 18(3), pp.234-237.

Teledyne Marine, 2017. ATLAS PARASOUND Deep-Sea Parametric Sub-Bottom Profiler. http://www.teledynemarine.com/parasound-sub-bottom-profilers?ProductLine ID=79/. Slangerup, Denmark (accessed 21 October 2022).

Thomas, F.C., Medioli, F.S. and Scott, D.B. 1990. Holocene and latest Wisconsinan benthic foraminiferal assemblages and paleocirculation history, lower Scotian slope and rise. Journal of Foraminiferal Research, 20, 3: 212-245.

Todd, R. and Low, D. 1981. Marine Flora and Fauna of the Northeastern United States. Protozoa: Sarcodina: Benthic Foraminifera. Series: NOAA technical report NMFS CIRC; 439. United States, National Marine Fisheries Service, https://repository.library.noaa.gov/view/noaa/5425.

Toomey, M.R., Korty, R.L., Donnelly, J.P., van Hengstum, P.J. and Curry, W.B., 2017. Increased hurricane frequency near Florida during Younger Dryas Atlantic meridional overturning circulation slowdown. Geology, 45(11), pp.1047-1050.

Trincardi, F., Cattaneo, A., Correggiari, A. and Ridente, D., 2004. Evidence of soft sediment deformation, fluid escape, sediment failure and regional weak layers within the late Quaternary mud deposits of the Adriatic Sea. Marine Geology, 213(1-4), pp.91-119.

Vacchi, M., Engelhart, S.E., Nikitina, D., Ashe, E.L., Peltier, W.R., Roy, K., Kopp, R.E. and Horton, B.P., 2018. Postglacial relative sea-level histories along the eastern Canadian coastline. Quaternary Science Reviews, 201, pp.124-146.

Van de Poll, H.W., 1989. Lithostratigraphy of the Prince Edward Island redbeds. Atlantic Geology, 25(1), pp.23-35.

Vilks, G. 1969. Recent foraminifera in the Canadian Arctic. Micropaleontology, 15, 1: 35-60.

Vilks, G. 1989. Ecology of recent foraminifera on the Canadian Continental Shelf of the Arctic Ocean. In Y. Herman (Ed.) “The Arctic Seas: Climatology, Oceanography, Geology, and Biology”, pp. 497-569, Van Nostrand Reinhold, New York.

Vilks, G., Deonarine, B., Wagner, F.J., and Winters, G.V. 1982: Foraminifera and Mollusca in surface sediments of southeastern Labrador Shelf. Geological Society of America Bulletin, 93: 225-238.

Williamson, M.A., Keen, C.E. and Mudie, P.J. 1984. Foraminiferal distribution on the continental margin off Nova Scotia. Marine Micropaleontology, 9: 219 239.:219 239.

Winsborrow, M.C., Andreassen, K., Corner, G.D. and Laberg, J.S., 2010. Deglaciation of a marine-based ice sheet: Late Weichselian palaeo-ice dynamics and retreat in the southern Barents Sea reconstructed from onshore and offshore glacial geomorphology. Quaternary Science Reviews, 29(3-4), pp.424-442.

Zecchin, M. and Rebesco, M., 2018. Glacigenic and glacimarine sedimentation from shelf to trough settings in the NW Barents Sea. Marine geology, 402, pp.184-193.

Zecchin, M., Rebesco, M., Lucchi, R.G., Caffau, M., Lantzsch, H. and Hanebuth, T.J., 2016. Buried iceberg-keel scouring on the southern Spitsbergenbanken, NW Barents Sea. Marine Geology, 382, pp.68-79.

Deglaciation history and relative sea level changes since the Last Glacial Maximum in the southern Gulf of St. Lawrence, Canada

I. Schulten[1*], V. Maselli[1, 2], E. L. King[3], M. Schmidt[4], C. Hensen[4], T. Müller[4, 5], A. Asioli[6], A. Micallef[7], C. Berndt[4], C. J. Brown[8], F. Córdoba-Ramírez[1], J. Elger[4, 9], S. Hölz[4], A. Kotliarov[10], B. Kurylyk[11], S. Yu[11], M. R. Nedimović[1]

[1] Department of Earth and Environmental Sciences, Dalhousie University, Halifax, Nova Scotia, Canada
[2] Department of Chemical and Geological Sciences, University of Modena and Reggio Emilia, Modena, Italy
[3] Natural Resources Canada (NRCan), Geological Survey of Canada Atlantic, Dartmouth, Nova Scotia, Canada
[4] GEOMAR Helmholtz Centre for Ocean Research Kiel, RD2/Marine Geosystems, RD4/Marine Geodynamic, Kiel, Germany
[5] Department Hydrogeology, Helmholtz Centre for Environmental Research GmbH - UFZ, Leipzig, Germany
[6] Institute of Marine Sciences (CNR-ISMAR), Bologna, Italy
[7] Monterey Bay Aquarium Research Institute (MBARI), Moss Landing, California, USA
[8] Department of Oceanography, Dalhousie University, Halifax, Nova Scotia, Canada
[9] Department of Geoscience, Aarhus University, Aarhus C, Denmark
[10] Fisheries and Marine Institute, Memorial University of Newfoundland, Newfoundland and Labrador, Canada
[11] Department of Civil and Resource Engineering and Centre for Water Resources Studies, Dalhousie University, Halifax, Nova Scotia, Canada

*Corresponding author: irena.schulten@dal.ca

Supplementary material

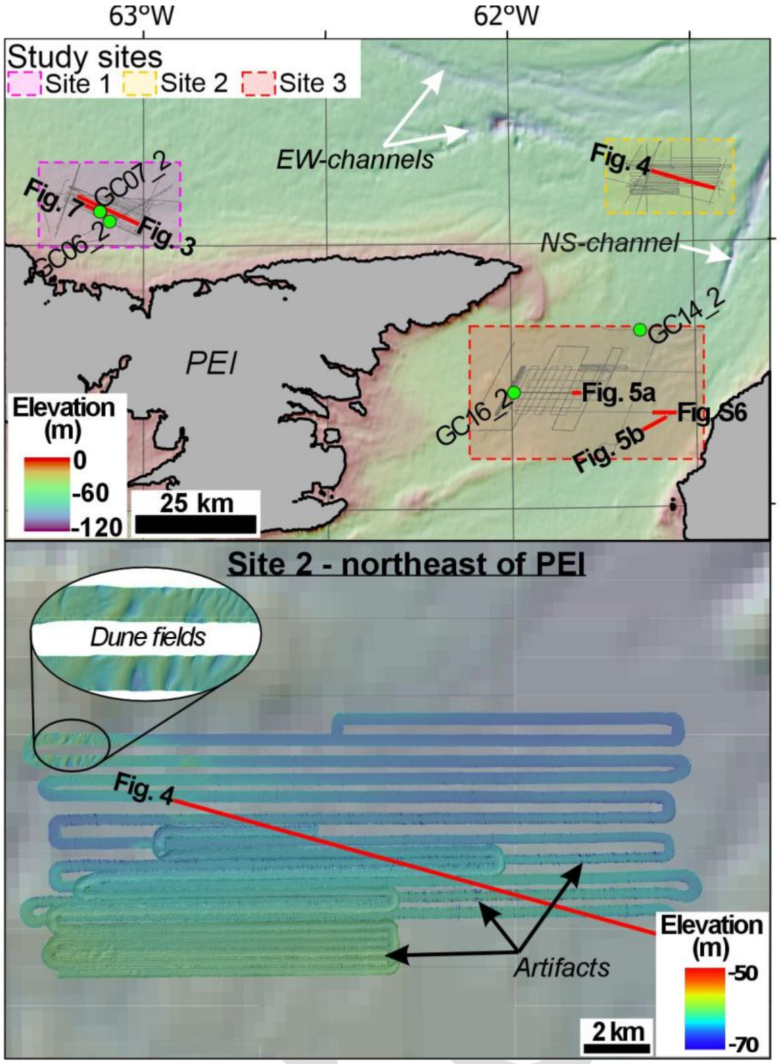

Fig. S1: Top: Overview of the study sites north (Site 1), northeast (Site 2) and east (Site 3) of PEI; and Bottom: multibeam bathymetry map of Site 2. Grey lines are sub-bottom profiles acquired during MSM103 and used in this study, while the red lines are the profiles presented in the figures. Green dots show the location of sediment cores (GC06_2, GC07_2, GC14_2, GC16_2) selected for this study. Morphologically significant sites and special characteristics are highlighted. The maps were generated using ArcGIS pro and background bathymetric data were downloaded from GEBCO. Please note that the multibeam data from Site 2 show numerous artifacts that could not be corrected with basic processing.

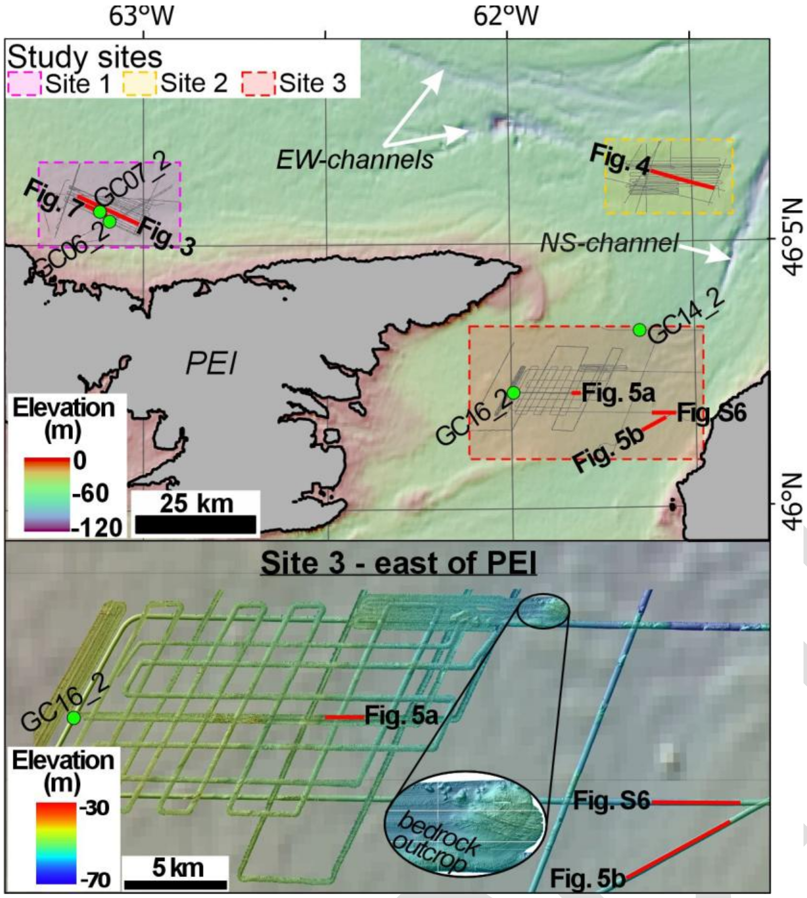

Fig. S2: Top: Overview of the study sites north (Site 1), northeast (Site 2) and east (Site 3) of PEI; and Bottom: multibeam bathymetry map of Site 3. Grey lines are sub-bottom profiles acquired during MSM103 and used in this study, while the red lines are the profiles presented in the figures. Green dots show the location of sediment cores (GC06_2, GC07_2, GC14_2, GC16_2) selected for this study. Morphologically significant sites and special characteristics are highlighted. The maps were generated using ArcGIS pro and background bathymetric data were downloaded from GEBCO. Please note that the multibeam data from Site 3 show numerous artifacts that could not be corrected with basic processing.

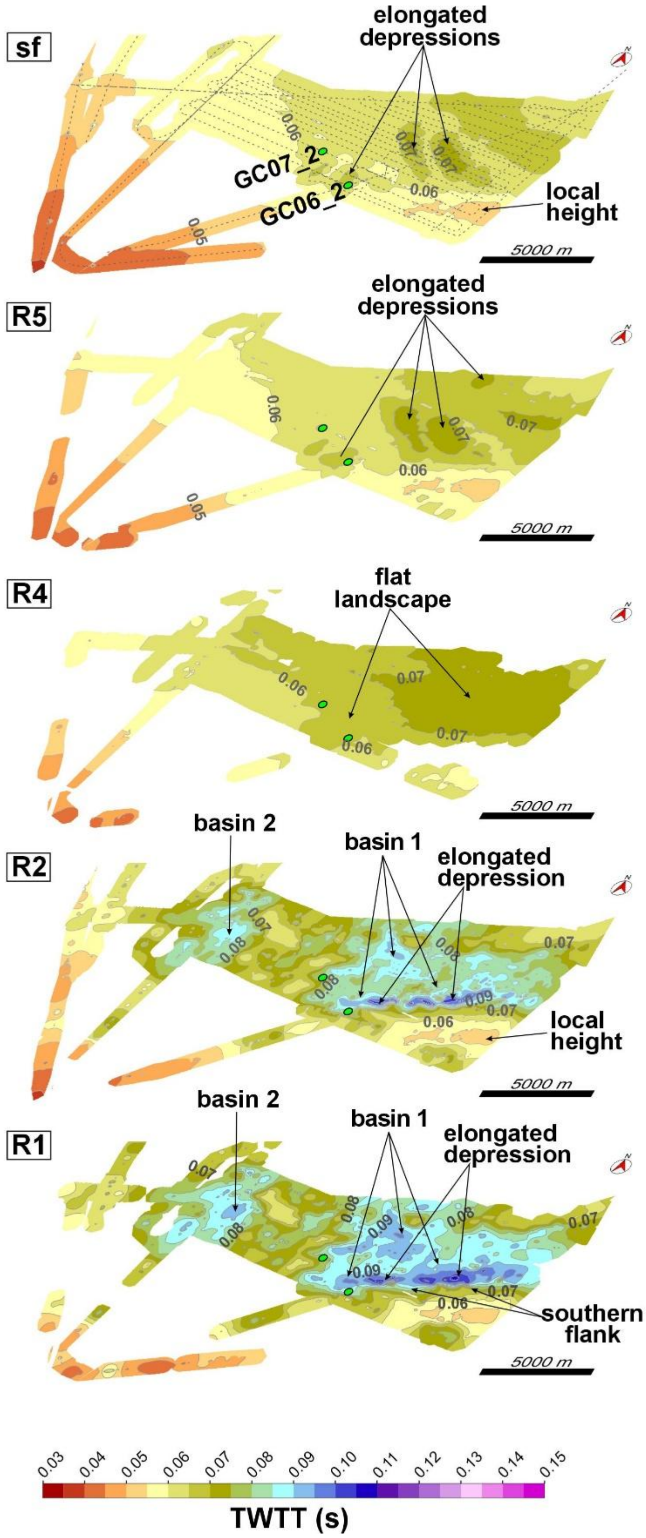

Fig. S3: Surface grids of reflection horizon R1, R2, R4, and R5 and the seafloor mapped within sub-bottom profiles in Site 1 in the Gulf of St. Lawrence north of PEI. Light green dots with black outlines show the location of sediment cores (GC06_2, GC07_2). Note that depth is in two-way-travel time (s) from sea level.

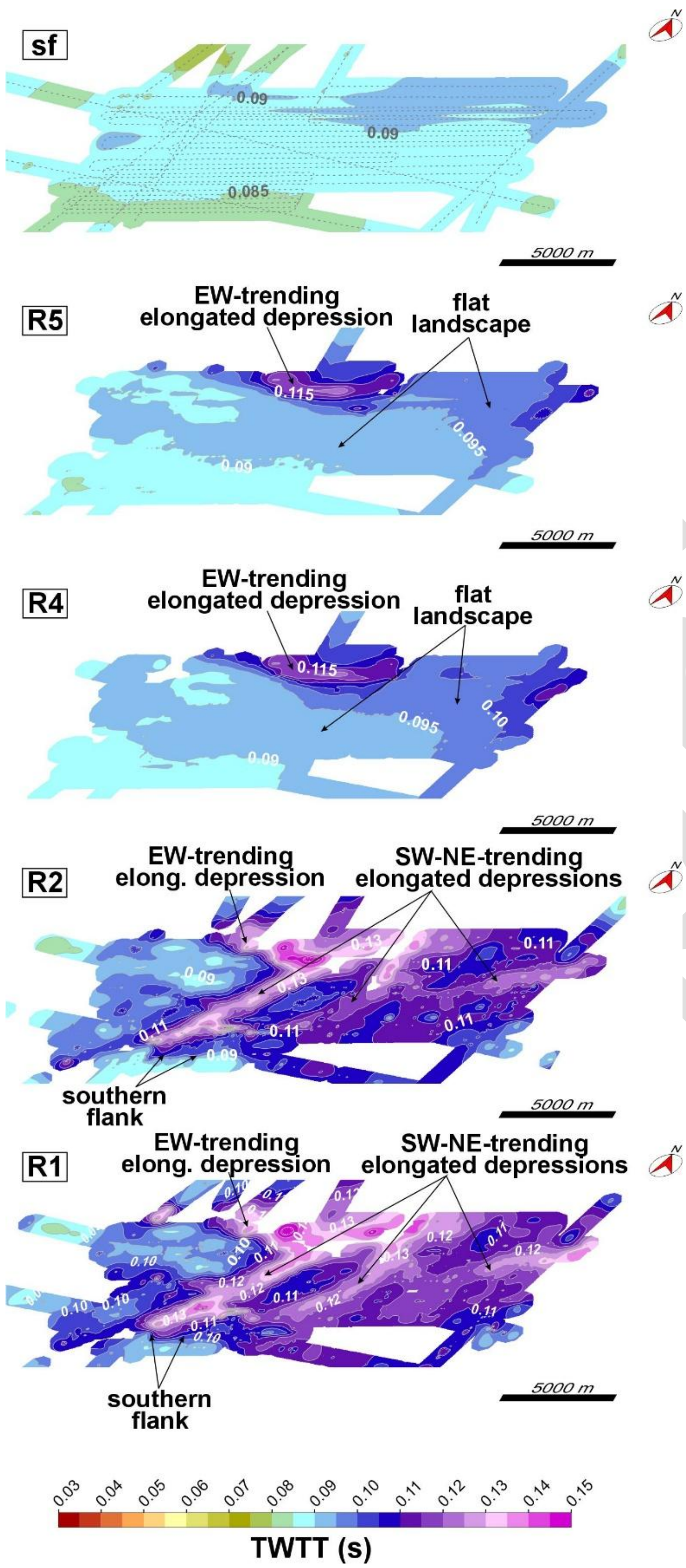

Fig. S4: Surface grids of reflection horizon R1, R2, R4, and R5 and the seafloor mapped within sub-bottom profiles in Site 2 northeast of PEI. Note that depth is in two-way-travel time (s) from sea level.

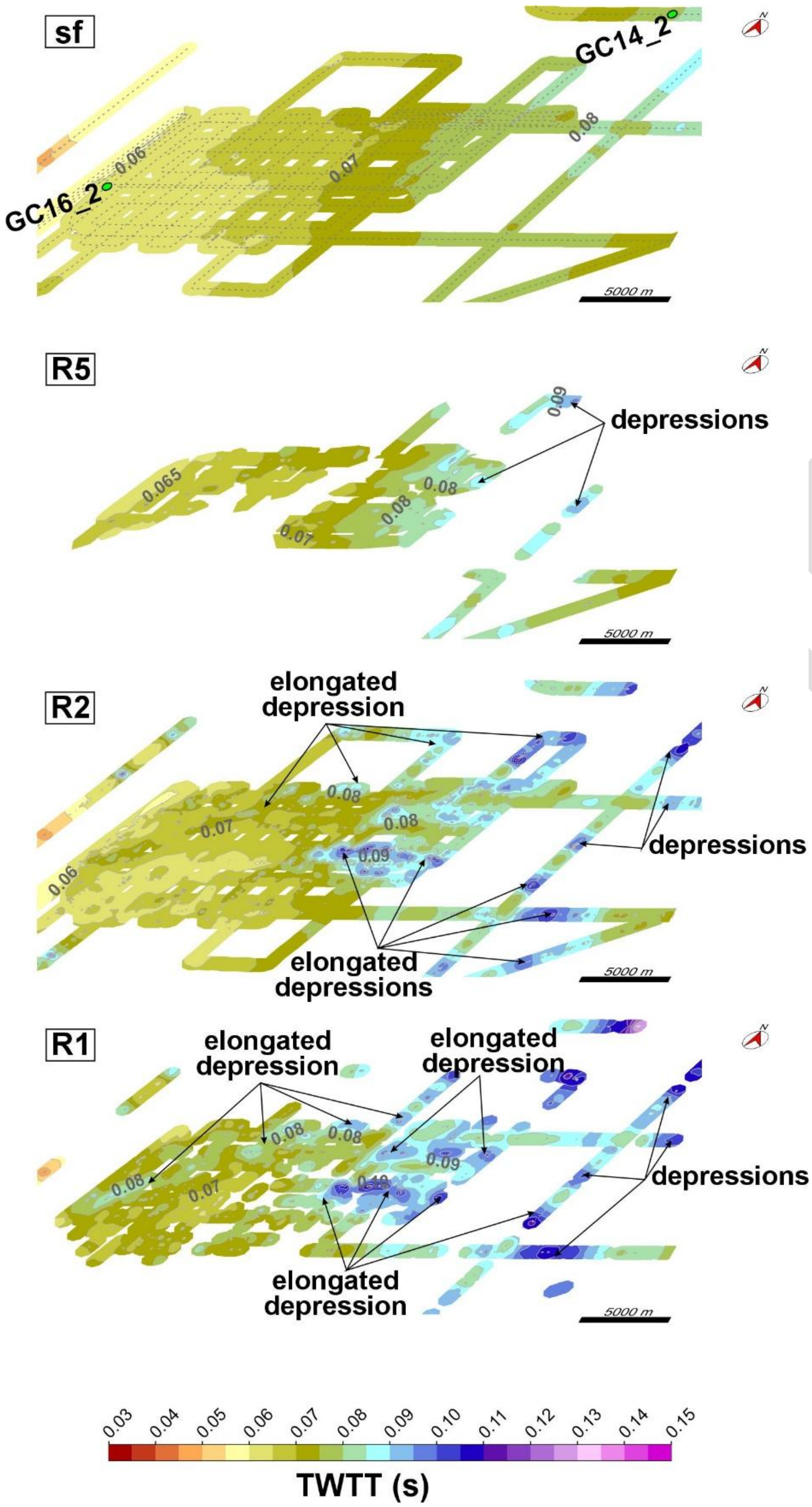

Fig. S5: Surface grids of reflection horizon R1, R2, and R5 and the seafloor mapped within sub-bottom profiles in Site 3 east of PEI. The light green dot with black outline shows the location of sediment core GC16_2. Note that depth is in two-way-travel time (s) from sea level.

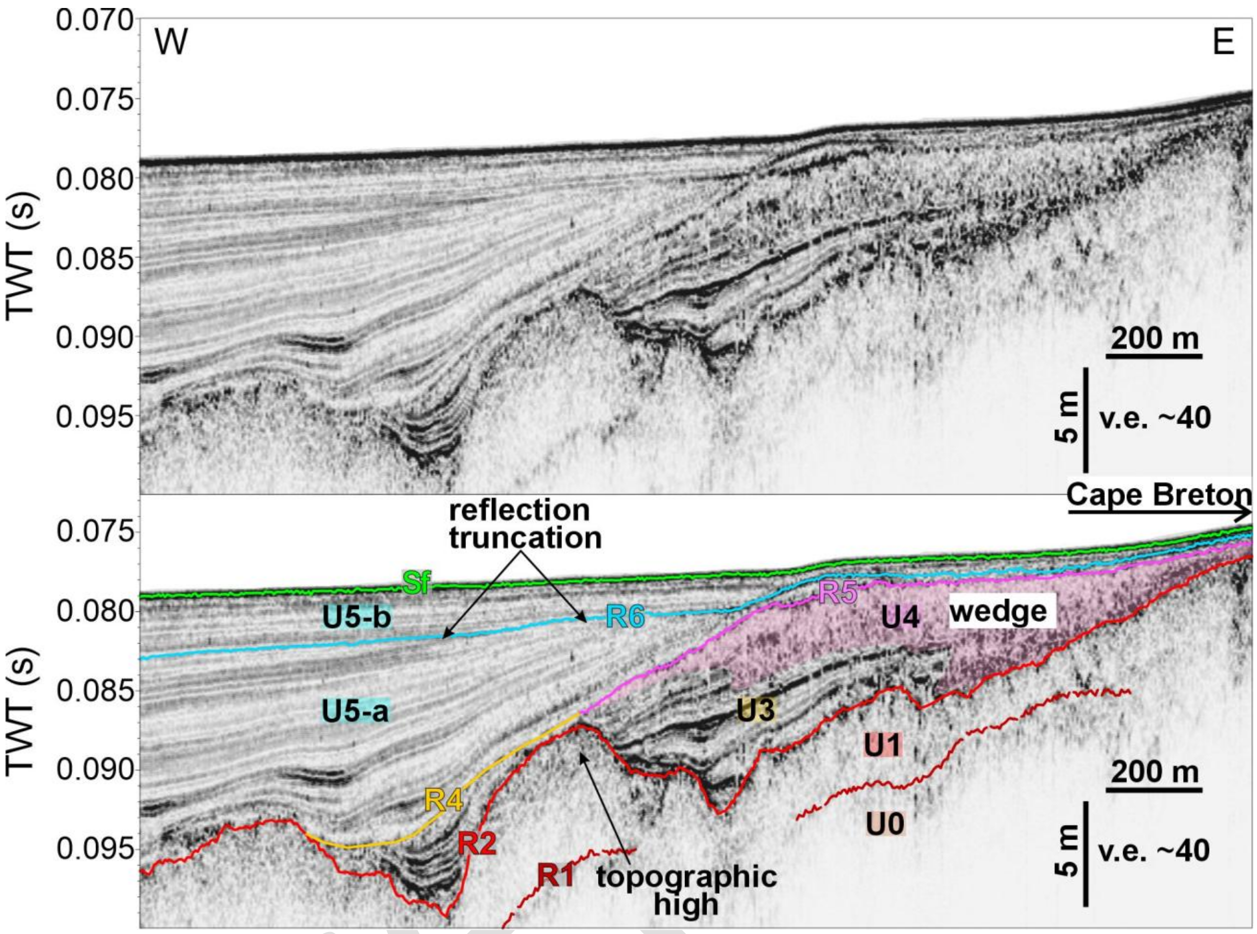

Fig. S6: W to E oriented sub-bottom profile acquired east of PEI in proximity to Cape Breton (Site 3, see Fig. 1b for location). The top image shows the uninterpreted profile, while the bottom image shows the interpretation. The distribution of key reflection horizons (R1-R6) and acoustic facies (U0-U5) as well as important reflection characteristics are highlighted. The pink polygon underlines the extent of U4, which in this profile appears wedge-shaped and intertwined with the underlying unit U3.

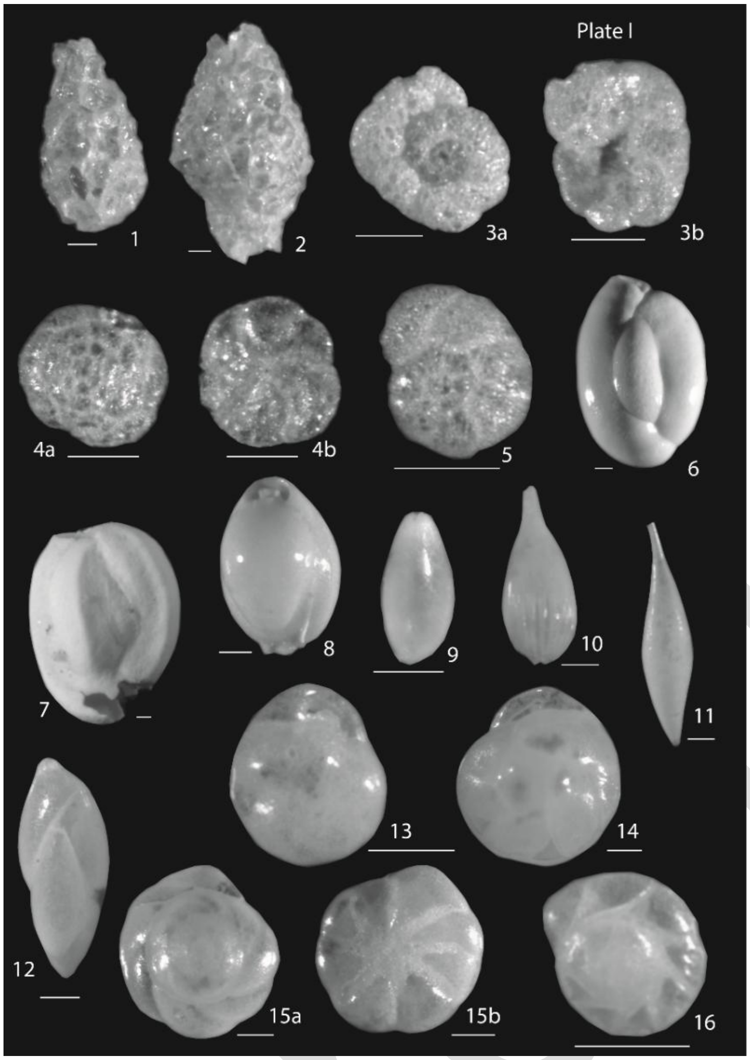

Plate I. 1) *Lagenammina atlantica* (Cushman, 1944) side view (sample GC16-2 cm 151.5-152.5); 2) *Reophax bilocularis* Flint, 1899 side view (sample GC16-2 cm 73-74); 3) *Trochammina squamata* Jones & Parker, 1860; a = dorsal view, b= ventral view (sample GC14-2 cm 306.5-307.5); 4) *Lepidodeuterammina ochracea* (Williamson, 1858); a = dorsal view, b= ventral view (sample GC14-2 cm 306.5-307.5); 5) *Trochammina nana* (Brady, 1881) dorsal view (sample GC14-2 cm 127.5-128.5); 6) *Quinqueloculina seminulum* (Linnaeus, 1758) side view (sample GC07-2 cm 78.5-79.5); 7) *Quinqueloculina stalkeri* Loeblich & Tappan, 1953 side view (sample GC14-2 cm 306.5-307.5); 8) *Pyrgo williamsoni* (Silvestri, 1923) side view (sample GC14-2 cm 306.5-307.5); 9) *Fissurina cucurbitasema* Loeblich & Tappan, 1953 peripheral view (sample GC07-2 cm 26.5-27.5); 10) *Lagena semilineata* Wright, 1886 side view (sample GC07-2 cm 78.5-79.5); 11) *Hyalinonetrion gracillimum* (Seguenza, 1862) side view (sample GC06-2 cm 277.5-278.5); 12) *Pseudopolymorphina novangliae* (Cushman, 1923) side view (sample GC06-2 cm 277.5-278.5); 13) *Cassidulina reniforme* Nørvang, 1945 side view (sample GC14-2 cm 127.5-128.5); 14) *Islandiella helenae* Feyling-Hanssen & Buzas, 1976 side view (sample GC14-2 cm 127.5-128.5); 15) *Buccella frigida* (Cushman, 1922) a = dorsal view, b= ventral view (sample GC06-2 cm 171.5-172.5); 16) *Epistominella exigua* (Brady, 1884) dorsal view (sample GC14-2 cm 127.5-128.5). Bar = 0.100 mm.

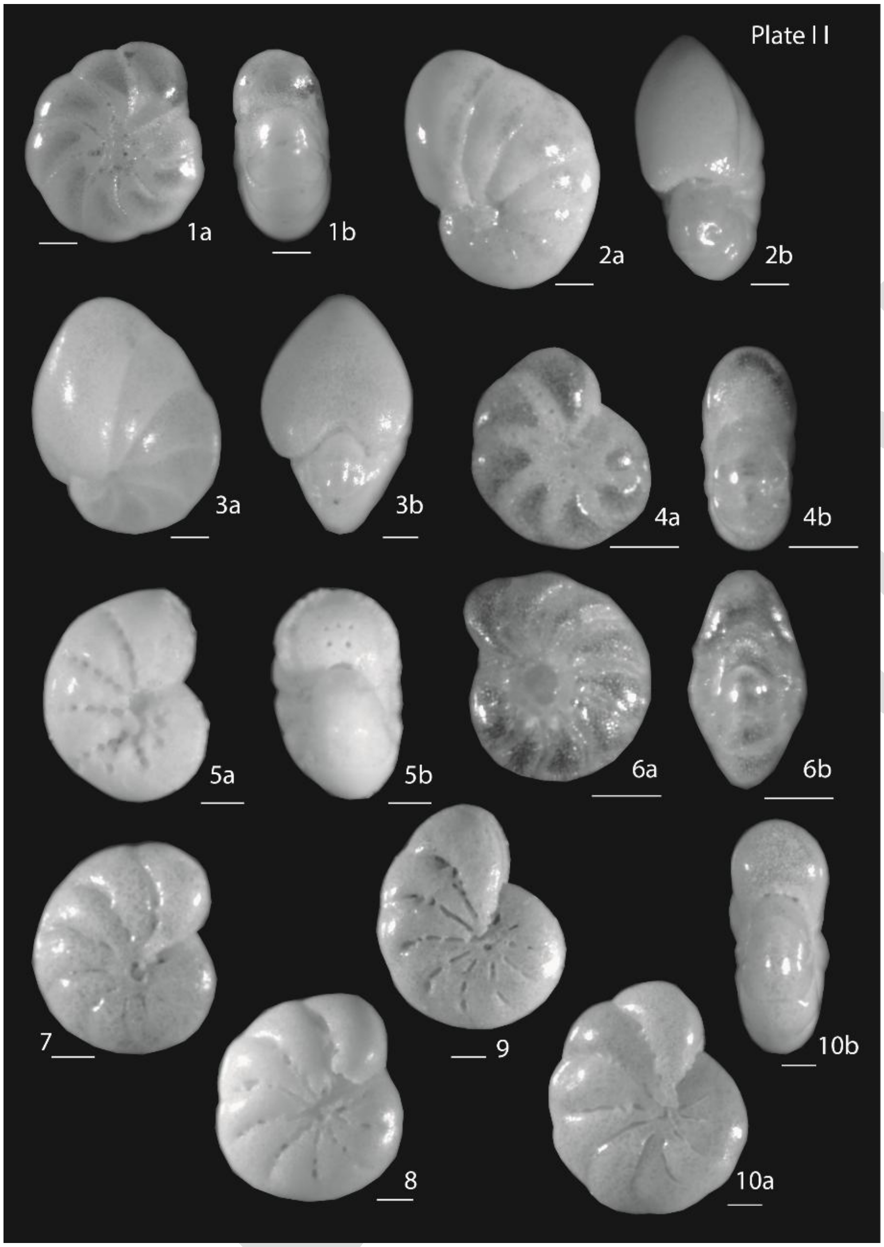

Plate II. 1) *Haynesina orbicularis* (Brady, 1881) a = side view, b = apertural view (sample GC06-2 cm 277.5-278.5); 2) *Nonionella auricula* Heron-Allen & Earland, 1930 a = side view, b = apertural view (sample GC14-2 cm 306.5-307.5); 3) *Nonionellina labradorica* (Dawson, 1860) a = side view, b = apertural view (sample GC14-2 cm 443.5-444.5); 4) *Elphidium frigidum* Cushman, 1933 a = side view, b = apertural view (sample GC06-2 cm 171.5-172.5); 5) *Elphidium bartletti* Cushman, 1933 a = side view, b = apertural view (sample GC14-2 cm 443.5-444.5); 6) *Elphidium clavatum* Cushman, 1930 a = side view, b = apertural view (sample GC06-2 cm 171.5-172.5); 7-10) *Elphidium excavatum* (Terquem, 1875) side view, 10b = apertural view (sample GC07-2 cm 176.5-177.5). Bar = 0.100 mm.

Supplementary material, part 2:

Table S1: MSM103 taxa raw data.

Cruise MSM103																			
Core GC06-2			description of the examined fraction (>0.063mm)																
#sample	sample depth (cm)	dry weight (g)	terrigenous	vegetal remains	mollusks	ostracods	Forams	forams pres. state	*B. frigida*	*C. reniforme*	*E. bartletti*	*E. clavatum*	*E. excavatum*	*E. frigidum*	*E. macrescens*	*E. exigua*	*F. cucurbitasema*	*H. orbicularis*
1	46.5-47.5	53.086	A (red fine sand)	-	-	RR	R	VG	x	-	-	-	xx	-	-	-	-	xx
2	171.5-172.5	54.615	A (red fine sand)	-	-	R	C	VG	C/R	-	-	C	C	RR	-	-	-	C
3	277.5-278.5	63.265	A (red fine sorted sand)	-	-	C	C/R	VG	R	-	-	R	A	RR	-	-	-	C/R
Core GC07 -2																		
#sample	sample depth (cm)																	
1	26.5-27.5	51.108	C (red fine sorted sand)	-	-	R	R	VG	xx	-	-	x	xx	-	-	-	x	-
2	78.5-79.5	49.899	C(red fine sorted sand)	-	-	R	C	VG	C	-	-	C	C	-	-	-	-	R
3	176.5-177.5	55.427	C (red fine sorted sand)	-	-	C/R	C	VG	R	-	-	C	C	-	-	-	-	R
4	277.5-278.5	51.929	A (red fine sorted sand)	-	-	R	R	VG	x	-	-	xx	xx	-	-	-	-	x
5	354.5-355.5	48.626	A (red fine sorted sand)	-	-	R	R	VG	x	-	-	xx	xx	-	-	-	-	x
Core GC14-2																		
#sample	sample depth (cm)																	
1	127.5-128.5	45.46	A (fine grey-reddish sorted sand)	C/R	-	-	RR	VG	x	x	-	-	x	-	x	x	-	-
2	306.5-307.5	44.201	C (fine grey-reddish sorted sand)	C/R	-	-	RR	VG	x	-	xx	xx	x	-	-	-	-	-
3	443.5-444.5	39.78	C (red fine sorted sand)	C	R	-	R	G	xx	-	x	xx	xx	-	-	-	-	-
Core GC16-2																		
#sample	sample depth (cm)																	
1	73-74	39.657	C (red fine sorted sand)	R	-	-	R	VG	-	-	-	-	-	-	-	-	-	-
2	151.5-152.5	58.433	A (red fine sorted sand)	R	R	-	C	VG	RR	-	-	-	R	-	-	-	-	-
3	206-207	59.462	AA (red fine sorted sand)	R	R	RR	C	VG	RR	-	-	C	A	-	-	-	-	R
4	278.5-279.5	50.247	AA (red fine sorted sand)	R	R	-	C	VG	-	-	-	A	A	-	-	-	-	R

H. gracillimum	*I. helenae*	*L. semilineata*	*L. atlantica*	*L. difflugiformis*	*L. ochracea*	*N. auricola*	*N. labradorica*	*P. novangliae*	*P. williamsoni*	*Q. seminulum*	*Q. stalkeri*	*R. bilocularis*	*Reophax* spp	*R. laevis*	*S. sphaerica*	*Spiroplectammina* spp	*T. inflata*	*T. nana*	*T. squamata*	BIOFACIES
-	-	-	-	-	-	-	-	-	-	-	-	-	-	-	-	-	-	-	-	A
-	-	-	-	-	-	-	-	RR	-	-	-	-	-	-	-	-	-	-	-	A
RR	-	-	-	-	-	-	-	RR	-	-	-	-	-	-	-	-	-	-	-	A
													-							
-	-	-	-	-	-	-	-	x	-	-	-	-	-	-	-	-	-	-	-	A
-	-	RR	-	-	-	-	-	RR	-	RR	-	-	-	-	-	-	-	-	-	A
-	-	-	-	-	-	-	-	-	-	-	RR	-	-	-	-	-	-	-	-	A
-	-	-	-	-	-	-	-	x	-	-	-	-	-	-	-	-	-	-	-	A
-	-	-	-	-	-	-	-	-	-	-	-	-	-	-	-	-	-	-	-	A
-	xx	-	-	-	x	-	x	-	-	-	-	-	-	-	-	-	-	x	x	B
-	xx	-	x	-	-	x	xx	-	x	-	-	-	-	-	-	-	-	-	-	B
-	x	-	-	-	x	x	xx	-	-	-	-	-	x	-	-	-	x	-	-	B
-	-	-	-	xx	-	-	-	-	-	-	-	xx	-	-	-	x	x	-	-	C
-	-	-	R	A	-	-	-	-	-	-	-	-	-	-	RR	-	-	-	-	C
-	-	-	RR	R	-	-	-	R	-	-	RR	-	-	-	-	-	-	-	-	A
-	-	-	-	-	-	-	-	RR	-	-	-	-	-	RR	-	-	-	-	-	A

Legend

sample description (fraction >0.063mm)	
AA	very abundant
A	abundant
C	common
R	rare
RR	very rare
-	absent
VG	very good
G	good
B	bad
xx	taxon present with some specimen in samples with R or RR forams
x	taxon present with one or two specimens in samples with R or RR forams
Foraminifera taxa	
B. frigida	*Buccella frigida* (Cushman, 1922)
C. reniforme	*Cassidulina reniforme* Nørvang, 1945
E. bartletti	*Elphidium bartletti* Cushman, 1933
E. clavatum	*Elphidium clavatum* Cushman, 1930
E. frigidum	*Elphidium frigidum* Cushman, 1933
E. excavatum	*Elphidium excavatum* (Terquem, 1875)
E. macrescens	*Entzia macrescens* (Brady, 1870)
E. exigua	*Epistominella exigua* (Brady, 1884)
F. cucurbitasema	*Fissurina cucurbitasema* Loeblich & Tappan, 1953
H. orbicularis	*Haynesina orbicularis* (Brady, 1881)
H. gracillimum	*Hyalinonetrion gracillimum* (Seguenza, 1862)
I. helenae	*Islandiella helenae* Feyling-Hanssen & Buzas, 1976
L. semilineata	*Lagena semilineata* Wright, 1886
L. atlantica	*Lagenammina atlantica* (Cushman, 1944)
L. difflugiformis	*Lagenammina difflugiformis* (Brady, 1879)
L. ochracea	*Lepidodeuterammina ochracea* (Williamson, 1858)
N. auricola	*Nonionella auricula* Heron-Allen & Earland, 1930
N. labradorica	*Nonionellina labradorica* (Dawson, 1860)
P. novangliae	*Pseudopolymorphina novangliae* (Cushman, 1923)
P. williamsoni	*Pyrgo williamsoni* (Silvestri, 1923)
Q. seminulum	*Quinqueloculina seminulum* (Linnaeus, 1758)
Q. stalkeri	*Quinqueloculina stalkeri* Loeblich & Tappan, 1953
R. bilocularis	*Reophax bilocularis* Flint, 1899
Reophax spp	
R. laevis	*Reussoolina laevis* (Montagu, 1803)
S. sphaerica	*Saccammina sphaerica* Brady, 1871
Spiroplectammina spp	
T. inflata	*Trochammina inflata* (Montagu, 1808)
T. nana	*Trochammina nana* (Brady, 1881)
T. squamata	*Trochammina squamata* Jones & Parker, 1860